# $Mn_2O_3$ oxide with bixbyite structure for the electrochemical oxygen reduction reaction in alkaline media : highly active if properly manipulated

# $Mn_2O_3$ oxide with bixbyite structure for the electrochemical oxygen reduction reaction in alkaline media: highly active if properly manipulated

Anna S. Ryabova[a,b], Sergey Ya. Istomin[a], Kirill A. Dosaev[a,b], Antoine Bonnefont[c], Joke Hadermann[d], Natalya A. Arkharova[e], Anton S. Orekhov[e], Robert Paria Sena[d], Viktoriia A. Saveleva[a,1], Gwénaëlle Kéranguéven[a,], Evgeny V. Antipov[b], Elena R. Savinova[a], Galina A. Tsirlina[b,2]

[a] *ICPEES, UMR 7515 CNRS-ECPM-Université de Strasbourg, 25, rue Becquerel, F 67087 Strasbourg Cedex 2, France*

[b] *Moscow State University, Faculty of Chemistry, Leninskie Gory, 1-str. 3, Moscow 119991, Russia*

[c] *IC, UMR 7177, CNRS- Université de Strasbourg, 4 rue Blaise Pascal, 67000 Strasbourg, France*

[d] *EMAT, University of Antwerp, Department of Physics, Groenenborgerlaan 171, B-2020 Antwerp, Belgium*

[e] *A.V. Shubnikov Institute of Crystallography FSRC "Crystallography and photonics" RAS, 59, Leninsky pr., 119333 Moscow, Russia*

**Abstract**

We consider compositional and structural factors which can affect the activity of bixbyite α-$Mn_2O_3$ towards the oxygen reduction reaction (ORR) and the stability of this oxide in alkaline solution. We compare electrochemistry of undoped, Fe and Al-doped α-$Mn_2O_3$ with bixbyite structure and braunite $Mn_7SiO_{12}$ having bixbyite-related crystal structure, using the rotating disk electrode (RDE), the rotating ring-disc electrode (RRDE), and cyclic voltammetry (CV) techniques. All manganese oxides under study are stable in the potential range between the ORR onset and ca. 0.7 V vs. Reversible Hydrogen Electrode

[1] Present address: European Synchrotron Radiation Facility (ESRF), 38000 Grenoble, France
[2] Corresponding author. E-mail: tsir@elch.chem.msu.ru

(RHE). It is found that any changes introduced in the bixbyite structure and/or composition of $\alpha$-$Mn_2O_3$ lead to an activity drop in both the oxygen reduction and hydrogen peroxide reactions in this potential interval. For the hydrogen peroxide reduction reaction these modifications also result in a change in the nature of the rate-determining step. The obtained results confirm that due to its unique crystalline structure undoped $\alpha$-$Mn_2O_3$ is the most ORR active (among currently available) Mn oxide catalyst and favor the assumption of the key role of the (111) surface of $\alpha$-$Mn_2O_3$ in the very high activity of this material towards the ORR.

**Keywords:** oxide electrocatalysts, $Mn_2O_3$, bixbyite structure, oxygen reduction reaction (ORR), hydrogen peroxide oxidation and reduction reactions

## 1. Introduction

Transition metal oxides (TMOs) are of high interest due to their catalytic activity towards the oxygen reduction reaction (ORR) in alkaline media and can be used as noble metal-free materials at the cathode of liquid and polymer electrolyte alkaline fuel cells [1-3] and metal-air batteries [4,5]. Manganese oxides stand out among other transition metal oxides [6], because of their high catalytic activity, stability in the potential range of the ORR, and low cost. Besides, manganese oxides are 'green' materials, which are widespread in nature. Numerous studies have been devoted to the investigation of manganese oxides in the ORR [7-14]. However, the results reported by different research groups are often contradictory, which is due to the dependence of the electrocatalytic activity on various intrinsic and extrinsic factors [15] and lack of common protocol for the evaluation of the ORR activity. As a consequence, the relationships between the structure and composition of manganese oxides, on the one hand, and their electrocatalytic activity on the other hand, are still not fully understood. This lack of understanding is hindering the development of knowledge-based strategies for the design of highly active ORR catalysts for various applications. In particular, the available data for $\alpha$-$Mn_2O_3$ with bixbyite structure [8-24] are often conflicting.

Recently, some of us reported on the high ORR activity of $\alpha$-$Mn_2O_3$ with bixbyite structure, largely exceeding the specific activity (measured per unit surface area of the oxide) of Mn oxides with other structure/composition [24]. By analyzing the $O_2$ reduction and $HO_2^-$ oxidation/reduction current-potential curves for a set of Mn oxides ($\beta$-$MnO_2$, $\alpha$-$Mn_2O_3$, $LaMnO_3$ and $\alpha$-MnOOH), and by combining RDE and RRDE measurements with microkinetic modeling, a tentative ORR mechanism was proposed consisting of five reaction steps:

(i) the surface Mn(IV)/Mn(III) red-ox transition, where $O_{ad}$ and $OH_{ad}$ species are coordinated to the Mn(IV) and Mn(III) surface sites respectively.

$$O_{ad} + H_2O + e^- \rightleftarrows OH_{ad} + OH^- \quad , \qquad (1)$$

(ii) the $O_2$ adsorption and desorption occurring concomitantly with an electron transfer on Mn(III) surface cations (the latter identified as active reaction centers):

$$O_2 + OH_{ad} + e^- \rightleftarrows O_{2,ad} + OH^- \quad , \qquad (2)$$

(iii) the reduction of $O_{2,ad}$ into adsorbed $HO_{2,ad}$:

$$O_{2,ad} + H_2O + e^- \rightleftarrows HO_{2,ad} + OH^- \quad , \qquad (3)$$

(iv) the desorption/adsorption of $HO_2^-$ from/on the Mn(III) surface site:

$$HO_{2,ad} + OH^- \rightleftarrows OH_{ad} + HO_2^- \quad , \qquad (4)$$

(v) the breaking of the O-O bond of $HO_{2,ad}$:

$$HO_{2,ad} + OH_{ad} \rightarrow 2O_{ad} + H_2O \quad . \qquad (5)$$

The differences in the electrocatalytic behavior of manganese oxides with various crystal structures could be correlated to their different kinetics of the oxygen reduction into hydrogen peroxide and of the hydrogen peroxide reduction into water. Furthermore, it was demonstrated that the ORR activity of Mn oxides correlates with the formal potential of the interfacial Mn(IV)/Mn(III) red-ox couple ($E_f$); $\alpha$-$Mn_2O_3$, with its highest $E_f$ in the series of studied Mn oxides, exhibiting the highest ORR activity. The high activity of $\alpha$-$Mn_2O_3$ was attributed to the particular crystal structure features of the oxygen-deficient fluorite-related bixbyite structure. This structure type is stabilized by the presence of large cations like Jahn-Teller Mn(III) thus hampering their oxidation to substantially smaller Mn(IV) cations (ionic radius r(Mn(III))= 0.645 Å, r(Mn(IV))= 0.53 Å, coordination number 6 [25]). This results in a high Mn(IV)/Mn(III) potential due to high ionicity of the Mn-O bond. While quantum-chemical calculations performed by Nikitina *et al.* [26] for the $\alpha$-$Mn_2O_3$ (111) and $\alpha$-MnOOH (110) plane (the best and the worst catalysts in the experimentally studied series, correspondingly) suggested that steps (ii) to (v) may not be elementary, they have provided further justification for the high activity of $\alpha$-$Mn_2O_3$.

In order to shed more light on the origin of the high ORR activity of the bixbyite structure, in this work, we compare the activity of undoped α-$Mn_2O_3$, Al(III) or Fe(III)-doped α-$Mn_2O_3$, and braunite ($Mn_7SiO_{12}$) with a bixbyite-related structure. Partial substitution of Mn with Al or Fe cations (with the same coordination numbers 6) results in $Mn_{2-x}A_xO_3$ oxides, A= Al or Fe [27, 28]. Cation substitution has been proposed as the means to affect red-ox behavior of transition metal oxides (and thus change their electrocatalytic and charge storage capability) via the so-called 'inductive' effect [29-31]. Fe(III) was selected considering its similar to Mn(III) ionic radius (r(Fe(III))= 0.645 Å [25]) facilitating cationic substitution (even if it cannot provide the same metal-oxygen distance as for Mn(III) in α-$Mn_2O_3$ with bixbyite structure, the latter being the consequence of the Jahn-Teller distortion). Fe(III) substitution is known to improve red-ox properties of α-$Mn_2O_3$ used as an 'oxygen carrier' for the so-called chemical looping applications in the gas phase, whereby an oxide in a higher oxidation state (e.g. α-$Mn_2O_3$) releases oxygen, which is then used to oxidize a fuel [32,33]. To close the cycle, an oxide in a lower oxidation state (e.g. $Mn_3O_4$) is then re-oxidized by oxygen.

Introduction of smaller cations like Al(III) (r(Al(III))= 0.535 Å [25]) was expected to exert the so-called negative chemical pressure effect on the neighboring Mn(III)-O interatomic distances, and thus to induce a positive shift of the red-ox potential ($E_f$) of the Mn(IV)/Mn(III) couple positive.

Note however that these anticipations were based on analogies with the bulk properties of 'dry' oxides, and are not necessarily operative for a 'wet' oxide/electrolyte interface. What is important is that Mn(III) substitution either by Al(III) or Fe(III) is capable to modify the properties of Mn(III) active centers in the bixbyite structure rather than to provide new catalytic centers. This assumption is based on the fact that Fe oxides are known

to be inferior ORR catalysts compared to Mn oxides, while Al oxides have never been reported as ORR catalysts [34,35].

In addition, in this work we have studied another oxide, braunite ($Mn_7SiO_{12}$) synthetic mineral, which contains Mn(III) cations, and comprises fragments of the bixbyite structure (Fig. 1) [36,37]. The tetragonal crystal structure of braunite can be considered as a stacking of $Mn(III)_8O_{12}$ (A-slabs) and $Mn(II)_2Mn(III)_4Si_2O_{12}$ slabs (B-slabs) along the *c*-axis. A-slabs are also present in the crystal structure of $\alpha$-$Mn_2O_3$, resulting in similar (100) planes in the braunite and bixbyite structure. One may speculate that Mn(III) cations in B-slabs should not be electrochemically active since oxygen atoms belonging to these $MnO_6$ octahedra have common corners with Si(IV) (tetrahedrally coordinated). Moreover, 1/3 of oxygen atoms belonging to $MnO_6$ octahedra from the A-slab have common corners with $SiO_4$ tetrahedra and may also be inactive in the ORR. However, the other 2/3 of Mn(III) cations of the A-slab are expected to be ORR-active. Thus, $Mn_7SiO_{12}$ represents an interesting oxide material to study correlations between the crystal structure arrangement of Mn cations and the ORR activity.

In this manuscript we study ORR activities of undoped, Fe- and Al-doped $Mn_2O_3$ with bixbyite structure and braunite $Mn_7SiO_{12}$ using RDE, and, for some compositions, also RRDE. We complement these data with the RDE study of hydrogen peroxide oxidation/reduction reactions (HPOR/HPRR) to clarify which ORR steps are sensitive to the composition and the structure of the oxide. We use cyclic voltammetry in supporting electrolyte (deaerated 1 M NaOH or 0.1 M KOH) as a convenient means for *in situ* characterization of interfacial properties of electrocatalytic materials, which allows to assess the potential of red-ox transition(s), the charge corresponding to the interfacial Mn(IV)/Mn(III) recharging (the latter being proportional to the total number of possible ORR active sites), as well as the electrochemical stability of materials. Finally, we apply kinetic

modeling in order to understand how structural/compositional changes affect various steps of the ORR mechanism.

The manuscript is organized as follows. After presenting the experimental and modeling details, in section 3.1 we present structural characterization, then in subsection 3.2.1 we briefly discuss ORR and HPRR/HPOR on α-$Mn_2O_3$ in alkaline media, compare it with other Mn oxides, and propose likely reasons for inconsistencies in the literature regarding the ORR activity of α-$Mn_2O_3$. Subsection 3.2.2 is devoted to the overview of changes induced by Al(III) and Fe(III) doping or by replacing bixbyite structure with that of braunite, while section 3.3 consider various materials in detail, by a combined experimental and modeling approach.

## 2. Experimental and computational details

### 2.1. Materials

Six α-$Mn_2O_3$ samples were studied and denoted as $Mn_2O_3$(1) – (6). $Mn_2O_3$(1) was obtained by aerosol spray-pyrolysis technique described in Ref [38]. $Mn_2O_3$(3) was obtained by the heat treatment of α-MnOOH in air at 240 °C [39]. $Mn_2O_3$(2) and substituted $Mn_{2-x}A_xO_3$ (A= Fe, Al) were obtained by the sol-gel method using polyacryamide gel [40]. In this method, stoichiometric mixtures of Fe or Al nitrates and Mn acetate were dissolved in water, thereafter an aqueous solution of ammonium citrate $(NH_3)_3$(Cit) was added. The amount of citrate was calculated according to the chelate formula $ML_n$, where M is the metal, n its valence, and L a ligand (citric acid). The pH of the prepared solution was adjusted to neutral by adding aqueous $NH_3$. After that, acrylamide and N′,N′-methylendiacrylamide in quantities of 5 and 1.02 g per 100 mL of solution were added. The resulting solution was heated to the boiling point until formation of a transparent gel, which was placed into a furnace and slowly

heated in air at 650 $^{o}$C for 1 h. The obtained powder was ground and heated at 800 $^{o}$C for 4 to 12h. $Mn_2O_3$(4) and $Mn_2O_3$(5) were obtained by milling of the commercially available α-$Mn_2O_3$ ("Reachim", Russia). $Mn_2O_3$(6) was obtained by calcinations of an amorphous product of co-proportionation of $Mn(CH_3COO)_2$ and $KMnO_4$ in aqueous solution in air at 550 °C for 12 h [41].

In order to prepare $Mn_7SiO_{12}$ with a high surface area, a new method has been developed. In this method, Mn acetate was first dissolved in a mixture of 10 mL of water and 10 mL of ethanol heated at 80 °C. Thereafter, tetraethyl orthosilicate (TEOS) and 10 mL of 25 % $NH_3$ (aq) were added under permanent stirring. The mixture was then stirred at 80 °C for 1 h. The precipitate was filtered, thoroughly washed with water and dried at 75 °C overnight. Finally, the powder was heated in air at 900 °C for 5h. The resulting XRD pattern is available in Fig. 5 and Fig. S1.1.

Carbons of the Sibunit family with the BET surface area 65 $m^2g^{-1}$ and 82 $m^2g^{-1}$ were used to prepare oxide/carbon composites for all Mn oxides except of $Mn_2O_3$(3) and $Mn_2O_3$(4). Sibunit carbon with the BET surface area 6 $m^2g^{-1}$ was used for preparing $Mn_2O_3$(4)/carbon composite. $Mn_2O_3$(3) was studied using Sibunit carbons with different BET surface areas, as indicated in the text.

### 2.2. Sample characterization

The X-ray powder diffraction (XRD) characterization of the phase composition was performed with a Huber G670 Image plate Guinier diffractometer ($CuK_{\alpha 1}$ radiation, curved Ge monochromator, image plate detector).

$N_2$ physisorption isotherms were measured with ASAP 2010 analyzer (Micromeritics, USA) and used to determine the specific surface area ($S_{BET}$) by multiple-point Brunauer-Emmett-Teller (BET) approach.

For the $Mn_2O_3$ and $Mn_{1.9}Fe_{0.1}O_3$ samples, high angle annular dark field scanning transmission electron microscopy (HAADF-STEM) images and STEM-EDX maps were obtained with an aberration-corrected ThermoFisher Titan 80-300 "cubed" electron microscope operated at 300 kV equipped with a Super-X detector.

For the $Mn_7SiO_{12}$ sample, TEM, HAADF-STEM images and EDX elemental mapping analysis were performed on a FEI Tecnai Osiris electron microscope operated at 200 kV equipped with a Super-X detector.

EELS spectra were collected using a JEOL2100F microscope operated at 200 kV equipped with a Gatan Imaging Filter spectrometer.

X-Ray Photoelectron Spectroscopy (XPS) measurements were performed in an ultra-high vacuum chamber (pressure <5 $10^{-6}$ Pa) equipped with a VG Microtech Clam2 electron analyzer and a dual anode (Al and Mg Kα) X-ray source. The surface atomic ratios were calculated based on the intensities of the XP spectra using the equation (6) [42]:

$$\frac{n_1}{n_2} = \frac{I_1/\sigma_1}{I_2/\sigma_2} \quad , \quad (6)$$

here $\frac{n_1}{n_2}$ is the atomic ratio of elements '1' and '2', $I$ is the spectral intensities, $\sigma$ is the photoelectric cross-section for the atomic orbital in question taken from [43].

### 2.3. Electrode preparation and electrochemical measurements

Oxide and carbon were ground in a mortar for preparing oxide/carbon composites with the loading 91 $\mu g \cdot cm^{-2}_{geo}$ of oxide and 91 $\mu g \cdot cm^{-2}_{geo}$ of carbon, deposited onto the glassy carbon (GC) disc embedded either in an RDE or an RRDE tip as a thin film from a water-based ink, and then an alkaline ionomer AS-4 from Tokuyama Company was added on top of the oxide/carbon film in order to preserve its integrity, as described in Ref. [24].

Electrochemical measurements were performed in a standard three-electrode cell at 25 °C using an Autolab potentiostat (PGSTAT302N) equipped with an analog scan generator. Most of the measurements were done in 1 M NaOH, but some were performed in 0.1 M KOH electrolyte. All parts of the electrochemical cell in contact with the alkaline electrolyte were designed from Teflon. The electrolyte was prepared from an extra pure NaOH solution (Acros Organics, 50 wt.% aqueous solution) and ultra-pure water (18.2 MΩ·cm, < 3 ppb TOC, Purelab) or 0.1 M KOH (SIGMA-ALDRICH, 18.2 MΩ, 0.2 μm filtered). The counter electrode was a Pt wire and the reference electrodes were Hg/HgO/1 M NaOH or Hg/HgO/0.1 M KOH electrodes (+0.93 V *vs.* RHE) depending on the electrolyte used. In what follows all potentials (*E*) are referred to the RHE scale. The electrolyte resistance determined from the high frequency part of the electrochemical impedance spectra (measured in the 1 Hz to 100 kHz range) was equal to ca. 15 Ω.

CVs of the oxide/carbon composites were acquired in $N_2$-purged 1 M NaOH electrolyte at a scan rate of 10 $mV \cdot s^{-1}$ with the anodic limit ranging from 1.125 to 1.145 V and various cathodic limits for determining cathodic stability in the potential interval relevant to the ORR. The experimental total charge $Q$ (that is the charge comprising both red-ox transition and double layer charging) of Mn oxides was obtained as half of the sum of the anodic and cathodic charge of a CV measured at $v$= 10 $mV \cdot s^{-1}$ with cathodic limit 0.65 V after subtraction of the carbon contribution and normalizing to the BET surface area of the oxide. For oxides with the bixbyite structure, $Q_{calc}$ was roughly estimated from the bulk density of Mn cations to the power 2/3,[3] and assuming a single-electron Mn(IV)/Mn(III) red-ox transition of all Mn cations exposed to the surface. In contrast, for braunite, two charge

[3] Such an approach is similar to the conventional procedure applied for the real surface area determination of polycrystalline materials, and assumes presence of various crystal faces at the surface of the oxide particles.

values are considered, the first one corresponding to the charge of all surface Mn(III) cations, while the second only considers Mn(III) cations of the A-slab.

The RDE voltammograms were performed in $O_2$-saturated or $H_2O_2$ containing electrolytes at rotation rates from 400 till 2500 rpm at a 10 $mV \cdot s^{-1}$ scan rate. The RRDE experiments were performed with a Pt ring, on which a potential of +1.23 V vs. RHE was applied to oxidize the eventual $HO_2^-$ intermediate species formed during the ORR. The $HO_2^-$ yield was determined from the disc $I_D$ and the ring $I_R$ current using the following equation:

$$\text{yield of } HO_2^- = 100 \frac{2I_R/N}{(I_D + \frac{I_R}{N})} \quad , \tag{7}$$

with $N$, the collection factor. $N$ represents the fraction of diffused species detected at the ring and was determined experimentally with the reversible $Fe(CN)_6^{3-}$/ $Fe(CN)_6^{4-}$ red-ox couple using a thin layer of Pt/C in 10 mM $K_3Fe(CN)_6$ in 1 M NaOH. The experimental value of $N$ was equal to 0.25, which is close to the theoretical value calculated from the RRDE geometry parameters [44].

To quantify the electrocatalytic activities, kinetic currents were calculated from RDE data (see details in Ref. [24]). Tafel plots were constructed from RDE voltammograms after subtraction of the background current, correction of mass transport influence and normalization to the BET surface area of the Mn oxides.

To evaluate the effect of high cathodic polarization on the ORR and HPRR/HPOR activity, $\alpha$-$Mn_2O_3$ was subjected to a notoriously low (0.3 V vs. RHE) potential for 1800 s in 1 M KOH. The working electrode was first immersed in the $N_2$-purged 0.1 M KOH electrolyte and CVs were recorded between 0.63 V and 1.13 V starting from 0.93 V vs. RHE at 10 $mV \cdot s^{-1}$. Then, the working electrode was removed from the $N_2$-purged cell and placed in the cell containing the same electrolyte but saturated with oxygen and a RDE experiment was performed at 10 $mV \cdot s^{-1}$ and 900 rpm. Immediately after that, chronoamperometry in $O_2$-

purged 0.1 M KOH electrolyte was performed at 0.3 V during 1800 seconds without rotation. Next, the working electrode was placed back in the cell purged with nitrogen and CV voltammograms were recorded again to reveal eventual changes in the CV. Finally, the working electrode was placed in the cell containing 0.1 M KOH electrolyte saturated with oxygen, and RDE measurements were performed at 10 $mV \cdot s^{-1}$ and 900 rpm in order to test whether the ORR activity was affected by the potential hold at 0.3 V vs RHE. Similar protocol was applied for the HPRR/HPOR stability study, except for 1 M NaOH being used as electrolyte and potential hold performed in an $N_2$-purged electrolyte.

### 2.4. Microkinetic modeling

The differences in the ORR kinetics on the various Mn oxides with bixbyite and braunite structures can be rationalized with the help of a microkinetic model, which was proposed in our previous publications (Refs. [45-47]). This model was able to reproduce semi-quantitatively the experimental ORR and HPRR current-potential curves on Mn oxides.

The reaction rates $\upsilon_X$ of steps (i)-(v) can be mathematically expressed assuming Langmuir adsorption isotherms, fast mass transport and Butler-Volmer equation for the electron transfer kinetics:

$$\upsilon_1 = k_1\theta_O \exp\left(-\frac{(1-\alpha)FE}{RT}\right) - k_{-1}(1-\theta_{O_2}-\theta_{HO_2}-\theta_O)\exp\left(\frac{\alpha FE}{RT}\right) \quad , \tag{8}$$

$$\upsilon_2 = k_2 C^b_{O_2,} (1-\theta_{O_2}-\theta_{HO_2}-\theta_O)\exp\left(-\frac{(1-\alpha)FE}{RT}\right) - k_{-2}\theta_{O_2}\exp\left(\frac{\alpha FE}{RT}\right) \quad , \tag{9}$$

$$\upsilon_3 = k_3\theta_{O_2} \exp\left(-\frac{(1-\alpha)FE}{RT}\right) - k_{-3}\theta_{HO_2}\exp\left(\frac{\alpha FE}{RT}\right) \quad , \tag{10}$$

$$\upsilon_4 = k_4 C^b_{HO_2^-} (1-\theta_{O_2}-\theta_{HO_2}-\theta_O) - k_{-4}\theta_{HO_2} \quad , \tag{11}$$

$$\upsilon_5 = k_5\theta_{HO_2}(1-\theta_{O_2}-\theta_{HO_2}-\theta_O) \quad , \tag{12}$$

where $k_x$ is the rate constant of step $x$, $\theta_i$ the coverage of adsorbed intermediate $i$, $C_i^b$, the bulk concentration of species $i$, $E$ the electrode potential. The meaning and the values of other parameters are given in Table 1.

Under steady-state conditions, the ORR kinetic currents can be simulated by solving the following set of equations:

$$\frac{d\theta_{O2}}{dt} = \nu_2 - \nu_3 = 0 \quad , \tag{13}$$

$$\frac{d\theta_{HO2}}{dt} = \nu_3 + \nu_4 - \nu_5 = 0 \quad , \tag{14}$$

$$\frac{d\theta_{O}}{dt} = 2\nu_5 - \nu_1 = 0 \quad . \tag{15}$$

The Faradaic current density of the ORR can then be expressed by:

$$j_F = -F(\Gamma_{geo}(\nu_1 + \nu_2 + \nu_3) \quad . \tag{16}$$

Here $\Gamma_{geo}$ refers to the number of Mn cations per geometric surface area of the electrode, $C_{O_2}^b$ is the bulk concentration of $O_2$, which was assumed equal to 0.84 mM. The rate constants for $Mn_2O_3$ entering the kinetic model are taken from Ref. [47] and are given in Table 1.

## 3. Results and discussion

### 3.1. Structural characterization

XRD patterns of $Mn_{2-x}A_xO_3$ (A= Al and Fe) studied in this work are shown in Fig. 2. All samples show cubic bixbyite structure. The unit cell parameter of Al-doped oxides decreases with x while nearly no change is observed for the Fe-doped ones. This is in accordance with ionic radii of Mn(III), Fe(III) and Al(III) cations discussed in the Introduction.

Figs. 3A and 3B show STEM images of $Mn_2O_3$(2) and $Mn_{1.9}Fe_{0.1}O_3$ samples. The $Mn_2O_3$(2) sample contains well-crystallized nanoparticles with the size ranging from 20 to 200 nm. High resolution HAADF-STEM images of several dozens of nanoparticles suggest that they prefer {111} facets (see Fig. 3A and Ref. [24]). It is interesting that introducing Fe in the bixbyite structure of $Mn_2O_3$, even at a low doping level, has a noticeable effect on the particle's shape. Indeed, HAADF-STEM images of $Mn_{1.9}Fe_{0.1}O_3$ show particles of mostly round (but also irregular) shape with no dominant facets (Fig. 3B). EDX-STEM quantification evidences very slight enrichment of the surface and subsurface region of the Fe-doped sample with Fe (Fig. 4, Fig. S2.1, Fig. S2.2). This slight surface enrichment with Fe was however not confirmed by the XPS analysis (Table 2), likely because of large error of the latter resulting from the low Fe content and the ensuing low intensity of the Fe2p peak (see Supporting Information). In the meantime, for the Al-doped samples XPS data evidence significant segregation of Al to the surface (Table 2).

The oxidation state of Mn in undoped and Al(Fe)-doped $Mn_2O_3$ (Table S3.1) was estimated from the Mn L3/L2 ratio obtained from Mn L2,3 edge EEL spectra (Fig. S3.1) following the procedure proposed in Ref. [48]. No influence of the doping on the average Mn oxidation state could be noticed within the error of the analysis (~0.3).

For $Mn_7SiO_{12}$ we have succeeded to develop a new synthetic procedure, which allows to prepare braunite powdered samples with high surface area. The XRD pattern of $Mn_7SiO_{12}$ sample prepared by hydrolysis of $Mn(CH_3COO)_2$ and TEOS mixture after final annealing in air at 900 ℃ for 5h (Fig. 5) was fully indexed with unit cell parameters a= 9.4231(2) Å, c= 18.710(5) Å in space group *I4₁/acd* [36]. The TEM study (Fig. S2.3) confirms the crystal structure of the phase.

Specific surface areas of Mn oxides were determined by low temperature nitrogen adsorption within BET approximation. Values of the BET surface area ($S_{BET}$) for the studied

oxides are given in Table 3. The table also comprises electrochemical data, which are discussed further in the text.

### 3.2. ORR activity of oxides with bixbyite and bixbyite-derived structure

#### 3.2.1. ORR and HPRR/HPOR activity of α-$Mn_2O_3$

Before presenting the results of this work regarding the activity of pristine and doped $Mn_2O_3$, we briefly summarize the previously published data. Fig. 6 shows ORR activity (calculated as kinetic ORR current at 0.9 V vs. RHE) of various Mn oxides and its correlation with the $E_f$. The activity span between the most active Mn oxide (α-$Mn_2O_3$) and the least active Mn oxide (α-MnOOH) is nearly two orders of magnitude, even if both oxides contain Mn cations in the same oxidation state (III). According to microkinetic modeling, the differences in the ORR kinetics of Mn oxides do not solely originate from different formal potential values (affecting the coverage of various adsorbates) but also from the structure-dependent rate constants of the reaction steps (ii), (iii) (corresponding to consecutive steps of oxygen reduction to hydrogen peroxide), and (v) (bond breaking in hydrogen peroxide ultimately leading to its transformation into water). Quantum chemical calculations of Nikitina *et al.* [26] have demonstrated the influence of surface structure-dependent adsorbate-adsorbate interactions on the activation barrier of the O-O bond breaking in the adsorbed hydrogen peroxide (in the considered ORR mechanism this corresponds to step (v), while quantum-chemical calculations suggest that this step involves $OH^-$ anion rather than $H_2O$ molecule formation [26]). Insets in Fig. 6 show model clusters constructed from the optimized "periodical" oxide surfaces of α-$Mn_2O_3$ and α-MnOOH (see Ref. [26] for detail). Shorter distance between surface Mn cations in α-$Mn_2O_3$ enables interaction of adsorbed OH and OOH (as well as O and OH), ultimately resulting in lowering of the activation barrier of

the bond-breaking step. Fast bond-breaking on the α-$Mn_2O_3$ surface translates in an effective four-electron transfer during the ORR and negligible amount of $H_2O_2$ detected at the ring in RRDE experiments. This does not necessarily mean that $H_2O_2$ is not formed as a reaction intermediate but rather that its subsequent transformation into water is very fast. This conclusion is confirmed by the fast electrocatalytic hydrogen peroxide reduction on α-$Mn_2O_3$ [47]. In the meantime, lack of OH and OOH (as well as O and OH) adsorbate-adsorbate interactions on the α-MnOOH surface translates in a high activation barrier of the O-O bond breaking, which experimentally manifests in kinetically-limited (rather than diffusion-limited as of α-$Mn_2O_3$) hydrogen peroxide reduction currents at high overpotentials and smaller number of electrons transferred in the ORR.

The ORR activity of α-$Mn_2O_3$ has been studied by several research groups. However, the reported activities vary substantially (Table S6.1). Various reasons may be responsible for such discrepancies (see Ref. [15]). In order to demonstrate this, in Fig. 7 we collected data (CVs, ORR RDE voltammograms, ORR Tafel plots, and HPRR/HPOR RDE voltammograms) for $Mn_2O_3$ samples with different BET surface areas ($S_{BET}$= 10 and 24 $m^2 \cdot g^{-1}$ for $Mn_2O_3$(4) and $Mn_2O_3$(3), correspondingly), combined with two different carbon materials (Sibunit-152 with $S_{BET}$= 65 $m^2 \cdot g^{-1}$ and Sibunit-176 with $S_{BET}$= 6 $m^2 \cdot g^{-1}$), measured in two different electrolytes (1 M NaOH and 0.1 M KOH) as is, and after polarization at 0.3 V vs. RHE. The purpose of this figure is to illustrate sensitivity of the ORR activity to various factors rather than to provide systematic analysis. For detailed information the reader is referred to original publications (*vide infra*). *First*, traces 1 and 2 in Fig. 7 demonstrate the influence of carbon on the CV and on the RDE voltammogram in $O_2$-saturated 1 M NaOH. Indeed, low electronic conductivity of α-$Mn_2O_3$ requires addition of carbon for its applications in electrochemistry. In the meantime, the type of carbon, its fraction, and the way it is introduced in the catalyst

(during the synthesis, by mixing, grinding, etc.) may change the electrocatalytic activity of $Mn_2O_3$ (and other transition metal oxides) [49-55] significantly (sometimes by order(s) of magnitude). One may see that low surface area carbon material ($S_{BET}$= 6 $m^2 \cdot g^{-1}$) in Fig. 7 does not allow to fully utilize the surface of the oxide (*cf.* charge under CVs in Fig. 7a) resulting in a lower activity. *Second*, traces 1 and 3 illustrate the influence of the supporting electrolyte (1 M NaOH vs. 0.1M KOH) both on the kinetic and on the diffusion limiting current. For more information on the effect of electrolyte pH and the nature of the alkali metal cation the reader is referred to Refs. [56,57]. *Third*, traces 3 and 4 illustrate the influence of cathodic degradation on the CV and on the ORR activity. One may notice that exposing $Mn_2O_3$ to polarization at 0.3 V vs. RHE for 1800 s significantly affects its CV and ORR activity (resulting in a two-fold activity loss) suggesting some irreversible transformations occurring at the oxide surface. Note that exposure to 0.3 V vs. RHE not only affects the ORR, but also the HPRR/HPOR kinetics (Fig. 7d). Hydrogen peroxide being the ORR intermediate, it is not surprising that the changes in the ORR and HPRR/HPOR are concurrent. It should be stressed that $Mn_2O_3$ (as well as other transition metal oxides) has its potential interval of stability, which is necessary to respect in order to obtain meaningful ORR activity data. According to Ryabova *et al.*, for $Mn_2O_3$ this stability interval spans from ca. 0.65 V to ca. 1.15 V vs. RHE, while for other Mn oxides it may even be narrower [24]. Analysis of the literature data confirms that this stability interval is not always respected (see Table S6.1). Reductive and oxidative degradation of $Mn_2O_3$ has been recently reported by Speck *et al.* [21] at low and high potentials, correspondingly. The authors studied oxide dissolution using an electrochemical on-line inductively coupled plasma mass spectrometry. In the absence of on-line spectroscopic tools, the oxide stability can be readily and conveniently tested by cyclic voltammetry. In order to investigate stability of $Mn_2O_3$ with respect to reduction, the lower potential limit was progressively decreased from 0.9 to 0.4 V

in 50 mV increments, while the anodic potential limit was kept constant at 1.145 V (see Fig. S5.4a in the SI and Fig. 4 from Ref. [24]). A pronounced irreversible reduction starts below ca. 0.65 V resulting in a modification of the shape of the CVs. As the cathodic potential limit in Fig. S5.4a is extended below 0.5 V vs. RHE, the CV changes become drastic, which signifies that the surface of the catalyst has been modified. Considering strong influence of the crystalline structure and composition on the electrocatalytic activity of Mn oxides (see e.g. Refs. [24,58]), it is not surprising that neglecting the stability interval may greatly affect the measured ORR activity. *Fourth*, several publications stress on the influence of morphology, the type of planes exposed to the surface, and presence of structural defects on the electrocatalytic activity [19,59,60]. Finally, the temperature may also influence the measured activity. In this context it is interesting to mention that α-$Mn_2O_3$ undergoes a phase transition from orthorhombic to cubic phase very near to room temperature, at 302 K (see Ref. [61] and references therein). According to the density functional theory (DFT) calculations of Henzie *et al.* [62] the orthorhombic phase is a narrow bandgap semiconductor, while the cubic α-$Mn_2O_3$ phase is a semimetal due to the mixing and overlap of the Mn 3d and O 2p orbitals. Furthermore, the authors observed a non-monotonous increase of the ORR activity of α-$Mn_2O_3$ with the temperature, which they attributed to the orthorhombic to cubic phase transition. It should be noted however that authors of Ref. [62] studied α-$Mn_2O_3$ without addition of carbon, which may be responsible for the ORR 'onset potential' much inferior of that reported by Ryabova *et al.* [24].

### 3.2.2. Structural/compositional changes in the bixbyite structure – influence on the ORR activity

Fig. 8a shows representative Tafel plots for $Mn_7SiO_{12}$, undoped $Mn_2O_3$ as well as Al- and Fe-doped $Mn_{2-x}A_xO_3$. Full set of RDE and background data can be found in SI. One may

see that undoped $Mn_2O_3$ samples exhibit the highest specific activity. The ORR activities of the $Mn_2O_3$(3) and $Mn_2O_3$(2) are lower than those of the most active $Mn_2O_3$(1), $Mn_2O_3$(5), $Mn_2O_3$(6) at 0.9 V, by 25 and 38%, respectively, which probably indicates that morphology is also important. While the differences are more pronounced at 0.9 V (Fig. 8a), the data in the Table 3 are given at 0.85 V in order to be able to compare their kinetic currents with less active doped materials. Both Al and Fe doping results in an ORR activity drop. However, their qualitative effect on the Tafel plot is different. While Al doping results in a downshift of the Tafel plot with a slight decrease of the slope, Fe-doping leads to bending of the plot, with a noticeable increase of the Tafel slope at higher overvoltage. The most significant changes in the Tafel plots and the most drastic activity loss in this series occur when bixbyite structure is replaced by the braunite one ($Mn_7SiO_{12}$).

To understand the possible origin of the activity losses, Tafel plots were simulated with the help of the kinetic model presented in section 2.4, the results are shown in Fig. 8b. The goal of this modeling was to describe semi-quantitatively a series of experimental Tafel plots of Fig. 8a in order to understand which ORR steps could be affected by the doping and/or structure change. In order to make kinetic simulations more reliable, we not only considered the ORR activities, but also the ORR selectivities (measured with the RRDE), HPOR/HPRR current-potential curves, and CVs. In what follows, we combine all available experimental and modeling results and seek to explain the influence of structure/composition in the following order: Al-doped $Mn_2O_3$, Fe-doped $Mn_2O_3$, and finally $Mn_7SiO_{12}$.

### 3.3. Understanding the influence of composition and structure on the ORR activity

#### 3.3.1. Al-doped $Mn_2O_3$ with bixbyite structure

Typical CVs for Al-doped Mn oxide/carbon composites in $N_2$-purged 1 M NaOH solutions in the potential interval from 0.53 to 1.125 V vs. RHE are displayed in Fig. 9a, and can be compared to CVs of the undoped $Mn_2O_3$ oxides prepared with different synthetic approaches (see SI). As mentioned in the introduction, *the potential of the interfacial Mn(IV)/Mn(III) transition* was found to be an important characteristic strongly affecting electrocatalytic properties of Mn oxides in the ORR. The red-ox peaks attributed to the surface Mn(IV)/Mn(III) transition can be clearly identified for Al-doped $Mn_2O_3$, with a formal potential $E_f$ (estimated from their CVs as a half-sum of the anodic and cathodic peak potentials) at ca. 0.98 V ± 0.02 V, which is close to the $E_f$ of the undoped bixbyite (see Table 3). Similar to the undoped $Mn_2O_3$, the CVs of the Al-doped samples were found to be stable at least in the potential range from 0.65 to 1.125 V (Fig. S5.2).

Another important characteristic is the *interfacial charge* ($Q$) (see Section 2.3), which is proportional to the number of rechargeable Mn(III) cations considered as active sites. In the case of $Mn_2O_3$, experimental $Q$ values for differently synthesized samples (Table 3) are smaller (1.5 to 2 times) than the charge $Q_{calc}$ calculated from the surface cation density. Even if we consider $Q$ at very low scan rates, we cannot achieve $Q_{calc}$. The difference between the experimental and the calculated charge may be related to an inequivalence of interfacial Mn cations. According to atomic level modeling of the surface relaxation of the slabs representing $Mn_2O_3$(111) surface [26]), some Mn cations become closer as compared to their usual positions in octahedra, and for some others the distance increases. We can assume that only some of these inequivalent Mn cations are able to recharge/protonate. Furthermore, $Mn_2O_3$ samples may differ in terms of preferred crystal plane orientation at the surface.

For Al-doped $Mn_2O_3$ oxides, the experimentally measured charge $Q$ is substantially smaller than for the undoped $Mn_2O_3$, which can be explained by segregation of Al to the surface evidenced by XPS (Table 2). This allows us to follow the behavior of bixbyite with essentially decreased number of surface Mn(III) cations available for recharging and thus for electrocatalysis. Considering XPS data enables correction of $Q_{calc}$ to the Mn fraction in Al-doped $Mn_2O_3$ (Table 3). One may see that, similar to what has been observed for the undoped $Mn_2O_3$, the measured charge for Al-doped $Mn_2O_3$ is 1.5 to 2 times inferior of the calculated one.

Tafel plots for the ORR on $Mn_{2-x}Al_xO_3$ and undoped $Mn_2O_3$, show similar slopes 85 – 90 mV/decade in the overall potential interval, but substantially (2-3 times) lower activities in the former case if kinetic current is normalized to the BET area of the oxide. This activity decrease is in agreement with the decrease of the number of Mn cations at the interface available to recharging and detected by CV. The Koutecky-Levich analysis (Fig. S7.1) reveals that the effective number ($n_{eff}$) of electrons transferred in the ORR at 0.65 V is close to 4 for both $Mn_2O_3$ and $Mn_{2-x}Al_xO_3$. This is in line with the results of RRDE experiment showing that the fraction of $HO_2^-$ intermediate escaping from the $Mn_{2-x}Al_xO_3$ catalyst layer during the ORR (Fig. 9 c,d,e) remains at a low level (ca. 4% below 0.85 V, as for $Mn_2O_3$ with a similar catalyst loading [26]). Note that the amount of $HO_2^-$ escaping the catalyst layer depends on the catalyst loading, BET area, and the density of active centers [26]. We avoid more detailed comparison because low peroxide yields cannot be determined with high accuracy.

The experimental data for undoped $Mn_2O_3$ can be well reproduced by microkinetic simulations considering the $E_f$ of 0.98 V, and fast kinetics for both $O_2$ reduction into $HO_2^-$ (steps (ii), (iii)) and $HO_2^-$ reduction into water (steps (i) and (v)) (see red curve in Fig. 8 and Refs. [24,26,47]). To simulate ORR data for $Mn_{2-x}Al_xO_3$ samples, we took into account the

unchanged $E_f$ value at ca. 0.98 V vs. RHE, similar Tafel slopes, and ca. 2 times smaller value of $Q$. The Tafel plots for $Mn_{2-x}Al_xO_3$ could be well reproduced with the microkinetic model (i)-(v) by using the same rate constant values as for $Mn_2O_3$ but considering a two-fold decrease of the number of active Mn sites (Fig. 8b, magenta curve), which is consistent with the $Q$ difference for $Mn_2O_3$ and $Mn_{2-x}Al_xO_3$ samples. Thus, doping $Mn_2O_3$ by Al mainly results in a decrease of the number of active centers and then of the ORR specific activity (in case it is normalized to the BET surface area). This is corroborated by Fig. 9b showing the experimentally observed correlation between the kinetic currents on $Mn_2O_3$ and Al-doped samples and $Q$ (proportional to the number of Mn(IV)/Mn(III) sites that are electrochemically active).

The scatter in Fig. 9b demonstrates that the number of rechargeable sites is an important but not an exclusive factor. One may notice that for Al-doped samples the data points are below the line, the downward deviation increasing with the Al content. We assume that another important factor may be interfacial acidity, which is higher for the Al oxide than for any of the Mn oxides [63]. We suppose that the close proximity to Al affects Mn-O protonation in a way less favorable for the ORR. This aspect requires a dedicated study in future.

#### 3.3.2. Fe-doped $Mn_2O_3$ with bixbyite structure

For Fe-doped $Mn_2O_3$ (Fig. 10a) red-ox peaks in CVs are very broad. Even if the exact value of $E_f$ cannot be determined, one may see that it is substantially lower than that of the undoped $Mn_2O_3$. Several reasons may be responsible for the different CV shape of Fe-doped $Mn_2O_3$ and for the negative shift of $E_f$ relative to the undoped one. *First*, the BET surface area of the Fe-doped $Mn_2O_3$ samples is much lower than that for $Mn_2O_3$(2), $Mn_2O_3$(3) and Al-doped $Mn_2O_3$, which might be one of the reasons for the subtle red-ox peaks. *Second*, as discussed above, the shape of Mn oxide particles seems to be also affected by the Fe doping:

while $Mn_2O_3$ particles are bound by {111} facets, particles of $Mn_{1.9}Fe_{0.1}O_3$ do not show preferential facets. *Finally*, Fe(III)-O bonds are shorter than Mn(III)-O bonds [61], which may lead to a change in the interfacial structure (even at a low Fe doping level), a concomitant change in the $E_f$ and peak broadening. The latter suggests the existence of long-range interactions in ensembles of interfacial ions of transition metals. Moreover, Fe-doping seems to reduce resistance of the bixbyite structure towards cathodic degradation (see Fig. S5.4 of the SI). $Q$ depends on the extent of Fe-doping (*cf.* Table 1). It is close to $Q_{calc}$ for $Mn_{1.9}Fe_{0.1}O_3$ and $Mn_{1.7}Fe_{0.3}O_3$ but significantly increases for $Mn_{1.5}Fe_{0.5}O_3$. In the latter case one cannot be sure that the high $Q$ is only due to interfacial processes or rather involves bulk intercalation processes. Note however that low BET surface area of Fe-doped $Mn_2O_3$ affects the precision of the $Q$ determination.

In comparison to Al, Fe doping has a more drastic influence on the ORR activity of $Mn_2O_3$. The $n_{eff}$ value estimated from Koutecky-Levich (KL) plots of RDE voltammograms for $Mn_{1.9}Fe_{0.1}O_3$ and $Mn_{1.5}Fe_{0.5}O_3$ decreases down to 3.5 at 0.65 V vs. RHE (Fig. S7), and the $HO_2^-$ yield determined from RRDE measurements is above 25% (Fig. 10), which is significantly higher than for the $Mn_2O_3$ sample with a similar BET surface area. However, no correlation is observed between the Mn:Fe ratio and the amount of peroxide detected at the ring. The high $HO_2^-$ yield can be related to the slower hydrogen peroxide reduction reaction on $Mn_{2-x}Fe_xO_3$ samples evidenced by Figs. 10e and S9.1. In addition, a pronounced change in the Tafel slope is observed for all of the Fe-doped oxide samples at potentials above 0.85 V (Fig. 8a). In our previous work [24], such Tafel slope change observed for a Mn perovskite was attributed to the occurrence of the Mn(IV)/Mn(III) red-ox transition in this potential range. Indeed, above the Mn(IV)/Mn(III) formal potential, the oxide surface is mostly covered by Mn(IV) surface sites that are assumed to be inactive for the adsorption of either $O_2$ or $HO_2^-$ and thus for the ORR (HPRR). When the potential is decreased, the gradual

conversion of Mn(IV) into Mn(III) surface sites (able to adsorb $O_2$ or $HO_2^-$) results in a fast increase of the ORR kinetic current (observed between 0.92 and 0.86 V for $Mn_{2-x}Fe_xO_3$ samples). Below $E_f$, when Mn(III) sites are predominant at the oxide surface, the ORR kinetic current is high and exhibits smooth increase with the overvoltage. This regime is observed below 0.86 V for $Mn_{2-x}Fe_xO_3$ samples, the Tafel slope in this potential range being similar to that of $Mn_2O_3$. This is in agreement with the shift of $E_f$ down to ca. 0.85 – 0.9 V as can be assumed from CVs in the supporting electrolyte. This interpretation is supported by the kinetic simulations showing a Tafel slope change in the potential range between 0.92 to 0.8 V when the formal potential is decreased from 0.98 V (case of $Mn_2O_3$, red curve) to 0.86 V (see blue and green curves in Fig. 8b). The microkinetic simulations allows to explore the influence of the $HO_2^-$ reduction kinetic (from $k_5$= 50 $s^{-1}$, blue curve to $k_5$= 0.5 $s^{-1}$, green curve in Fig. 8b) on the shape of the Tafel plot. While these curves nearly overlap in the low overpotential region, a significant decrease of the ORR activity is observed in the high overpotential region when $k_5$ is decreased. Based on the simulations, the observed drastic difference between $Mn_2O_3$ and Fe-doped samples may be attributed to a slower $HO_2^-$ reduction ($k_5$ decrease) and a change of the Mn red-ox properties in $Mn_{1-x}Fe_xO_3$ ($E_f$ decrease). While the influence of Fe on the red-ox behavior of the $Mn_2O_3$ oxide has already been reported in high temperature 'looping' applications [32,33], in case of electrochemistry in an aqueous electrolyte one should also consider possible influence of the Fe doping on surface protonation/deprotonation equilibria. In this context it is interesting to note that the isoelectric point of maghemite $Fe_2O_3$ (4-6 [64]) is significantly lower than that of either bixbyite $Mn_2O_3$ (7.5 [65], 9.1 [66]) or $Al_2O_3$, which may result in a lower surface coverage of adsorbed OH species, the latter playing an essential role in the ORR mechanism, in particular by decreasing the barrier for the O-O bond breaking (step 5) in adsorbed hydrogen peroxide (*vide supra*).

### 3.3.3. $Mn_7SiO_{12}$ with bixbyite-derived structure

CVs of $Mn_7SiO_{12}$ after subtraction of the carbon contribution (Fig. 11a) exhibit broad weakly defined peaks, with a formal potential $E_f$ roughly estimated as 0.86 V, which is significantly lower than that of $Mn_2O_3$ (Table 3). This reveals that the red-ox Mn(IV)/Mn(III) properties are strongly affected when switching from the bixbyite to the braunite structure. The charge value ($Q$), characterizing accessible Mn(III) sites is rather close to the monolayer charge ($Q_{calc}$) estimated from crystallographic data taking into account that only Mn(III) cations belonging to the A-slab (the latter also present in the bixbyite structure) are active. No evidence of the $Mn_7SiO_{12}$ instability in alkaline solution was found since 1 month expose of the oxide to 1M NaOH did not lead to material degradation as confirmed by XRD (Fig. S1.1) and TEM (Fig. S2.4) studies.

The ORR activity of $Mn_7SiO_{12}$ is lower than of $Mn_2O_3$ by an order of magnitude (Fig. 8 a). The effective number ($n_{eff}$) of electrons transferred in the ORR is 3.3 (even lower than for Fe-doped Mn oxide), and the rate of the HPRR on this oxide (Fig. 11b) is also much slower than on $Mn_2O_3$(3) (trace 3 of Fig. 7d) despite their similar BET surface areas (*cf.* Table 3). The Tafel plot displayed in Fig. 8a exhibits a slope of around 88 mV/decade. In contrast to $Mn_{1-x}Fe_xO_3$ samples, no Tafel slope change could be observed experimentally in the potential range between 0.92 and 0.8 V. This absence of the Tafel slope change might be due to the low ORR activity of $Mn_7SiO_{12}$, which is largely dominated by the carbon contribution in the oxide/carbon composite [50]. The lower ORR activity of $Mn_7SiO_{12}$ might also stem from lower rate for steps (ii) and (iii), as confirmed by the microkinetic simulation (see orange curve in Fig. 8b).

## 4. Conclusions

α-$Mn_2O_3$ has a unique structure, which is responsible for the high formal potential of the surface Mn(IV)/Mn(III) transition, high rate constant for the hydrogen peroxide reduction, and high ORR activity. High variability in the values of ORR kinetic currents reported in the literature may be (at least partly) attributed to the absence of well-defined testing protocols, the measurements often being performed outsides the potential interval of $Mn_2O_3$ stability, without optimization of the carbon binder, and its fraction.

Our attempts to modify the structure and/or composition of $Mn_2O_3$ lead to an activity drop in both the oxygen and in the hydrogen peroxide reduction. It was found that partial replacement of Mn by Al cations in $Mn_2O_3$ leads to a significant change in the number of active surface Mn sites, which can be attributed to Al segregation to the surface confirmed by XPS. Al doping, while decreasing the number of active Mn sites, modifies their red-ox properties only slightly. In contrast, Fe doping modifies the potential of the interfacial Mn(IV)/Mn(III) transition and slows down the reduction of $HO_2^-$ to $OH^-$. The influence of Fe on the red-ox properties is in agreement with previous publications related to utilization of Fe-doped $Mn_2O_3$ as an oxygen carrier for high temperature applications. Another contribution may come from the change of the particle shape in Fe-doped $Mn_2O_3$ from well-defined {111} crystal planes at the surface of $Mn_2O_3$ to round particles with no preferential orientation. Finally, Fe might affect the extent of the surface protonation due to different acidity of the OH bound to either Fe or Mn. Braunite $Mn_7SiO_{12}$, a 2D analogue of byxbite $Mn_2O_3$, demonstrates low activity in the reduction of hydrogen peroxide, but also the lowest ORR activity most likely due to reduction of the activity of Mn(III) sites.

We believe that ORR electrocatalysis by oxides is a multifactorial phenomenon, which cannot be characterized by a single formal descriptor. Our general approach to the

problem consists in an experimental search for the key observable factors directly related to the oxide/solution interface The recharging behavior of the oxide in supporting electrolytes allows to extract two important parameters, namely the number of rechargeable centers and their formal potential, the latter controlling the relative contribution of transition metal cations in the active state ((III) for Mn) at the ORR onset.

**Acknowledgements:**

The authors are indebted to P.A. Simonov from the Boreskov Institute of Catalysis of the Russian Academy of Sciences for providing samples of carbon materials. The authors gratefully acknowledge V. Papaefthymiou and C. Ulhaq-Bouillet for the XPS and EELS measurements, respectively. Financial support from RFBR (research project No18-29-12064_mk) is greatly appreciated. A.R. and K.D thank French Embassy for PhD scholarships.

**Additional information:**

Electronic Supplementary Information (SI) is available.

Credit_authors_statement

Anna S. Ryabova: electrochemistry (bixbyite), editing,
Sergey Ya. Istomin: synthesis and XRD,
Kirill A. Dosaev: synthesis and electrochemistry (braunite),
Antoine Bonnefont: simulations, conceptualization
Joke Hadermann: TEM and local analysis (bixbyite),
Natalya A. Arkharova: TEM (braunite),
Anton S. Orekhov: TEM (braunite),
Robert Paria Sena: TEM and local analysis (bixbyite),
Viktoriia A. Saveleva: XPS analysis,
Gwénaëlle Kéranguéven: BET, EELS,
Evgeny V. Antipov: XRD methodology, reviewing,

Elena R. Savinova: conceptualization, methodology, writing-reviewing, editing

Galina A. Tsirlina: conceptualization, methodology, writing-reviewing, editing

**Declaration of interests**

The authors declare that they have no known competing financial interests or personal relationships that could have appeared to influence the work reported in this paper.

**References**

1 Z. Zhang, J. Liu, J. Gu, J.L. Su, L. Cheng, An overview of metal oxide materials as electrocatalysts and supports for polymer electrolyte fuel cells, Energy Environ. Sci. 7 (2014) 2535.

2 F. Cheng, J. Chen, Metal-air batteries: from oxygen reduction electrochemistry to cathode catalysts, Chem. Soc. Rev. 41 (2012) 2172.

3 J.W.D. Ng, Y. Gorlin, T. Hatsukade, T.F. Jaramillo, A precious-metal-free regenerative fuel cell for storing renewable electricity, Adv. Energy Mater. 3 (2013) 1545.

4 V. Neburchilov, H. Wang, J.J. Martin, W. Qu, A review on air cathodes for zinc–air fuel cells, J. Power Sources 195 (2010) 1271.

5 H. Osgood, S.V. Devaguptapu, H. Xu, J. Cho, G. Wu, Transition metal (Fe, Co, Ni, and Mn) oxides for oxygen reduction and evolution bifunctional catalysts in alkaline media, Nano Today 11 (2016) 601.

6 K.A. Stoerzinger, M. Risch, B. Han, Y. Shao-Horn, recent insights into manganese oxides in catalyzing oxygen reduction kinetics, ACS Catal. 5 (2015) 6021.

7 H.N. Cong, P. Chartier, J. Brenet, Réduction électrocatalytique de I'oxygène sur électrodes solides d'oxydes mixtes contenant des ions manganèse. II. Rôle du couple $Mn^{3+}$ - $Mn^{4+}$ en sites octaédriques, J. Appl. Electrochem. 7 (1977) 395.

8 L.Q. Mao, D. Zhang, T. Sotomura, K. Nakatsu, N. Koshiba, T. Ohsaka, Mechanistic study of the reduction of oxygen in air electrode with manganese oxides as electrocatalysts, Electrochim. Acta 48 (2003) 1015.

9 W.G. Hardin, J.T. Mefford, D.A. Slanac, B.B. Patel, X. Wang, S. Dai, X. Zhao, R.S. Ruoff, K.P. Johnston, K.J. Stevenson, Tuning the electrocatalytic activity of perovskites through active site variation and support interactions, Chem. Mater. 26 (2014) 3368.

10 F. Cheng, Y. Su, J. Liang, Z. Tao, J. Chen, $MnO_2$-based nanostructures as catalysts for electrochemical oxygen, Chem. Mater. 22 (2010) 898.

11 A.C. Garcia, A.D. Herrera, E.A. Ticianelli, M. Chatenet, C. Poinsignon, Evaluation of several carbon-supported nanostructured Ni-doped manganese oxide materials for the electrochemical reduction of oxygen, J. Electrochem. Soc. 158 (2011) B290.

12 Q.W. Tang, L.H. Jiang, J. Liu, S.L. Wang, G.Q. Sun, Effect of surface manganese valence of manganese oxides on the activity of the oxygen reduction reaction in alkaline media, ACS Catal. 4 (2014) 457.

13 F.H.B. Lima, M.L. Calegaro, E.A. Ticianelli, Electrocatalytic activity of manganese oxides prepared by thermal decomposition for oxygen reduction, Electrochim. Acta 52 (2007) 3732.

14 I. Roche, E. Chainet, M. Chatenet, J. Vondrak, Carbon-supported manganese oxide nanoparticles as electrocatalysts for the oxygen reduction reaction (ORR) in alkaline medium: physical characterizations and ORR mechanism, J. Phys. Chem. C 111 (2007) 1434.

15 A. Bonnefont, A.S. Ryabova, T. Schott, G. Kéranguéven, S.Y. Istomin, E.V. Antipov, E.R. Savinova, Challenges in the understanding oxygen reduction electrocatalysis on transition metal oxides, Curr. Opin. Electrochem. 14 (2019) 23.

16 W. Wang, J. Geng, L. Kuai, M. Li, B. Geng, Porous $Mn_2O_3$: a low cost electrocatalyst for oxygen reduction reaction in alkaline media with comparable activity to Pt/C, Chem. Eur. J. 22 (2016) 9909.

17 K.K. Hazarika, C. Goswami, H. Saikia, B.J. Borah, P. Bharali, Cubic $Mn_2O_3$ nanoparticles on carbon as bifunctional electrocatalyst for oxygen reduction and oxygen evolution reactions, Mol. Catal. 451 (2018) 153.

18 F. Cheng, J. Shen, W. Ji, Z. Tao, J. Chen, Selective synthesis of manganese oxide nanostructures for electrocatalytic oxygen reduction, ACS Apl. Mater. Interfaces 1 (2009) 460.

19 Y. Fang, Y. Wang, F. Wang, J. Zhu, 3D structured $Mn_2O_3$ synthesized using tween surfactant: influence on the morphology and oxygen reduction catalytic performance, CrystEngComm 21 (2019) 420.

20 M. Qasim, J. Hou, M.A. Qadeer, S. Butt, M.H. Farooq, M.Q. Farooq, F. Idrees, M. Tanveer, J. Zou, M. Tahir, Nitrogen-doped carbon nanosheets decorated with $Mn_2O_3$ nanoparticles for excellent oxygen reduction reaction, Front. Chem. 7 (2019) 741.

21 F.D. Speck, P.G. Santori, F. Jaouen, S. Cherevko, Mechanisms of manganese oxide electrocatalysts degradation during oxygen reduction and oxygen evolution reactions, J. Phys. Chem. C 123 (2019) 25267.

22 S. Cao, N. Han, J. Han, Y. Hu, L. Fan, C. Zhou and R. Guo, Mesoporous hybrid shells of carbonized polyaniline/$Mn_2O_3$ as non-precious efficient oxygen reduction reaction catalyst, ACS Appl. Mater. Interfaces 8 (2016) 6040.

23 Y. Gorlin, T.F. Jaramillo, A bifunctional nonprecious metal catalyst for oxygen reduction and water oxidation, J. Amer. Chem. Soc. 132 (2010) 13613.

24 A.S. Ryabova, F.S. Napolskiy, T. Poux, S.Y. Istomin, A. Bonnefont, D.M. Antipin, A.Y. Baranchikov, E.E. Levin, A.M. Abakumov, G. Kéranguéven, E.V. Antipov, G.A. Tsirlina, E.R. Savinova, Rationalizing the influence of the Mn(IV)/Mn(III) red-ox transition on the electrocatalytic activity of manganese oxides in the oxygen reduction reaction, Electrochim. Acta 187 (2016) 161.

25 R.D. Shannon, Revised effective ionic radii and systematic studies of interatomic distances in halides and chalcogenides, Acta Cryst. A 32 (1976) 751.

26 V.A. Nikitina, A.A. Kurilovich, A. Bonnefont, A.S. Ryabova, R.R. Nazmutdinov, E.R. Savinova, G.A. Tsirlina, ORR on simple manganese oxides: molecular-level factors determining reaction mechanisms and electrocatalytic activity, J. Electrochem. Soc. 165 (2018) J3199.

27 T. Ranganathan, B.E. MacKean, A. Muan, The system manganese oxide–alumina in air, J. Am. Ceram. Soc. 45 (1962) 279.

28 A. Muan, S. Somiya, The system iron oxide-manganese oxide in air, Am. J. Sci. 260 (1962) 230.

29 H. Zhu, S. Zhang, Y.X. Huang, L. Wu, S. Sun, Monodisperse $M_xFe_{3-x}O_4$ (M= Fe, Cu, Co, Mn) nanoparticles and their electrocatalysis for oxygen reduction reaction, Nano Lett. 13 (2013) 2947.

30 D.A. Kuznetsov, B. Han, Y. Yu, R.R. Rao, J. Hwang, Y. Roman-Leshkov, Y. Shao-Horn, Tuning Redox transitions via inductive effect in metal oxides and complexes, and implications in oxygen electrocatalysis, Joule 2 (2018) 225.

31 X. Han, B. Wang, C. Yang, G. Meng, R. Zhao, Q. Hu, O. Triana, M. Iqbal, Y. Li, A. Han, J. Liu, Inductive Effect in Mn-Doped NiO Nanosheet Arrays for Enhanced Capacitive and Highly Stable Hybrid Supercapacitor, ACS Appl. Energy Mater. 2 (2019) 2072.

32 M. Rydén, H. Leion, T. Mattisson, A. Lyngfelt, Combined oxides as oxygen-carrier material for chemical-looping with oxygen uncoupling, Catal. Today 285 (2017) 104.

33 E. Bazhenova, K. Honkala, Screening the bulk properties and reducibility of Fe-doped $Mn_2O_3$ from first principles calculations, Catal. Today 285 (2017) 104.

34 H. Wang, M. Zhou, P. Choudhury, H. Luo, Perovskite oxides as bifunctional oxygen electrocatalysts for oxygen evolution/reduction reactions – A mini review, Appl. Mater. Today 16 (2019) 56.

35 Y. Dessie, S. Tadesse, R. Eswaramoorthy, B. Abebe, Recent developments in manganese oxide based nanomaterials with oxygen reduction reaction functionalities for energy conversion and storage applications: a review, J. Sci. Adv. Mater. Devices 4 (2019) 353.

36 P.B. Moore, T. Araki, Braunite: its structure and relationship to bixbyite, and some insights on the genealogy of fluorite derivative structures, Am. Mineral. 61 (1976) 1226.

37 J.P. De Villiers, P.R. Buseck, Stacking variations and nonstoichiometry in the bixbyite-braunite polysomatic mineral group, Am. Mineral. 74 (1989) 1325.

38 S.H. Ju, D.Y. Kim, H.Y. Koo, S.K. Hong, E.B. Jo, Y.C. Kang, The characteristics of nano-sized manganese oxide particles prepared by spray pyrolysis, J. Alloys Compd. 425 (2006) 411.

39 V.M.B. Crisostomo, J. K. Ngala, S. Alia, A. Dobley, C. Morein, C.-H. Chen, X. Shen, S.L. Suib, New Synthetic Route, characterization, and electrocatalytic activity of nanosized manganite, Chem. Mater. 19 (2007) 1832.

40 A. Douy, Polyacrylamide gel: an efficient tool for easy synthesis of multicomponent oxide precursors of ceramics and glasses, Int. J. Inorg. Mater. 3 (2001) 699.

41 X. Cao, N. Wang, L. Wang, C. Mo, Y. Xu, X. Cai, L. Guo, A novel non-enzymatic hydrogen peroxide biosensor based on ultralong manganite MnOOH nanowires, Sens. Actuators B Chem.147 (2010) 730.

42 P. van der Heide, X-Ray Photoelectron Spectroscopy: an introduction to principles and practices, John Wiley & Sons, 2011.

43 J.J. Yeh, Atomic calculation of photoionization cross-sections and asymmetry parameters, Gordon & Breach Science, 1993.

44 A.J. Bard, L.R. Faulkner, Electrochemical methods - fundamentals and applications - 2nd ed. Wiley (USA), 2001.

45 T. Poux, A. Bonnefont, A. Ryabova, G. Kéranguéven, G.A. Tsirlina, E.R. Savinova, Electrocatalysis of hydrogen peroxide reactions on perovskite oxides: experiment versus kinetic modeling, Phys. Chem. Chem. Phys. 16 (2014) 13595.

46 T. Poux, A. Bonnefont, G. Kéranguéven, G.A. Tsirlina, E.R. Savinova, Electrocatalytic oxygen reduction reaction on perovskite oxides: series versus direct pathway, ChemPhysChem 15 (2014) 2108.

47 A.S. Ryabova, A. Bonnefont, P. Zagrebin, T. Poux, R.P. Sena, J. Hadermann, A.M. Abakumov, G. Kéranguéven, S.Y. Istomin, E.V. Antipov, G.A. Tsirlina, E.R. Savinova,

Study of hydrogen peroxide reactions on manganese oxides as a tool to decode the oxygen reduction reaction mechanism, ChemElectroChem 3 (2016) 1667.

48 H. Tan, J. Verbeeck, A. Abakumov, T. Van, Oxidation State and Chemical shift Investigation in Transition Metal Oxides by EELS, Ultramicroscopy 116 (2012) 24.

49 A. Flegler, S. Hartmann, H. Weinrich, M. Kapuschinski, J. Settelein, H. Lorrmann, G. Sextl, Manganese oxide coated carbon materials as hybrid catalysts for the application in primary aqueous metal-air batteries, C 2 (2016) 4.

50 T. Poux, F.S. Napolskiy, G. Kéranguéven, S.Y. Istomin, G.A. Tsirlina, E.V. Antipov, E.R. Savinova, Dual role of carbon in the catalytic layers of perovskite/carbon composites for the electrocatalytic oxygen reduction reaction. Catal. Today 189 (2012) 83.

51 S. Malkhandi, P. Trinh, A.K. Manohar, K.C. Jayachandrababu, A. Kindler, G.K.S. Prakash, S.R. Narayanan, Electrocatalytic activity of transition metal oxide-carbon composites for oxygen reduction in alkaline batteries and fuel cells, J. Electrochem. Soc. 160 (2013) F943.

52 W. Hardin, T.J. Mefford, D.A. Slanac, B.B. Patel, X. Wang , S. Dai , X. Zhao, R. Ruoff , K.P Johnston, K.J. Stevenson, Tuning the electrocatalytic activity of perovskites through active site variation and support interactions, Chem. Mater. 26 (2014) 3368.

53 A.S. Ryabova, A. Bonnefont, P.A. Simonov, T. Dintzer, C. Ulhaq-Bouillet, Y.G. Bogdanova, G.A. Tsirlina, E.R. Savinova, Further insights into the role of carbon in manganese oxide/carbon composites in the oxygen reduction reaction (ORR) in alkaline media, Electrochim. Acta 246 (2017) 643.

54 G. Kéranguéven, C. Ulhaq-Bouillet, V. Papaefthimiou, S. Royer, E. Savinova, Perovskite/carbon composites synthesized through in situ autocombustion for the oxygen reduction reaction: the carbon effect, Electrochim. Acta 245 (2017) 156.

55 P.-C. Li, C.-C. Hu, H. Noda, H. Habazaki, Synthesis and characterization of carbon black/manganese oxide air cathodes for zinc-air batteries: effects of the crystalline structure of manganese oxides, J. Power Sources 298 (2015) 102.

56 R.N. Singh, M. Malviya, Anindita, A.S.K.Sinh, P. Chartier, Polypyrrole and $La_{1-x}Sr_xMnO_3$ ($0 \leq x \leq 0.4$) composite electrodes for electroreduction of oxygen in alkaline medium, Electrochim. Acta 52 (2007) 4264.

57 J. Suntivich, E.E. Perry, H.A. Gasteiger, Y. Shao-Horn, The influence of the cation on the oxygen reduction and evolution activities of oxide surfaces in alkaline electrolyte, Electrocatalysis 4 (2013) 49.

58 Y. Meng, W. Song, H. Huang, Z. Ren, S.-Y. Chen, S.L. Suib, Structure−Property relationship of bifunctional $MnO_2$ nanostructures: highly efficient, ultra-stable electrochemical water oxidation and oxygen reduction reaction catalysts identified in alkaline media, J. Am. Chem. Soc. 136 (2014) 11452.

59 J.V. Swetha, H. Parse, B. Kakade, A. Geetha, Morphology dependent facile synthesis of manganese oxide nanostructures for oxygen reduction reaction, Solid State Ion. 328 (2018) 1.

60 M. Jahan, S. Tominaka, J. Henzie, Phase pure α-$Mn_2O_3$ prisms and their bifunctional electrocatalytic activity in oxygen evolution and reduction reactions, Dalton Trans. 45 (2016) 18494.

61 S. Geller, Structure of α-$Mn_2O_3$, $(Mn_{0.983}Fe_{0.017})_2O_3$ and $(Mn_{0.37}Fe_{0.63})_2O_3$ and relation to magnetic ordering, Acta Crystallogr. B 27 (1971) 821.

62 J. Mokkath, M. Jahan, M. Tanaka, S. Tominaka, J. Henzie, Temperature-Dependent Electronic Structure of Bixbyite α-$Mn_2O_3$ and the Importance of a Subtle Structural Change on Oxygen Electrocatalysis, ChemRxiv (2019) 1. https://doi.org/10.26434/chemrxiv.7716590.v1.

63 M. Kosmulski, The pH dependent surface charging and points of zero charge.VII. Update, Adv. Colloid Interface Sci. 251 (2018) 115.

64 R.C. Plaza, J.L. Arias, M. Espın, M.L. Jimenez, A.V. Delgado, Aging Effects in the Electrokinetics of Colloidal Iron Oxides, J. Colloid Interface Sci. 245 (2002) 86.

65 S. D. Škapin, V. Čadež, D. Suvorov, I. Sondi, Formation and properties of nanostructured colloidal manganese oxide particles obtained through the thermally controlled transformation of manganese carbonate precursor phase, J. Colloid Interface Sci. 457 (2015) 35.

66 G. Qi, C. Hai, Y. Shen, J. Zeng, X. Li, X. Ren, Y. Sun, S. Dong, Y. Zhou, Synthesis of mono-dispersed mesoporous $Mn_2O_3$ powders with micronanostructure for removing Congo red dye from aqueous solution, Adv. Powder Technol. 30 (2019) 930.

**Captions to Figures**

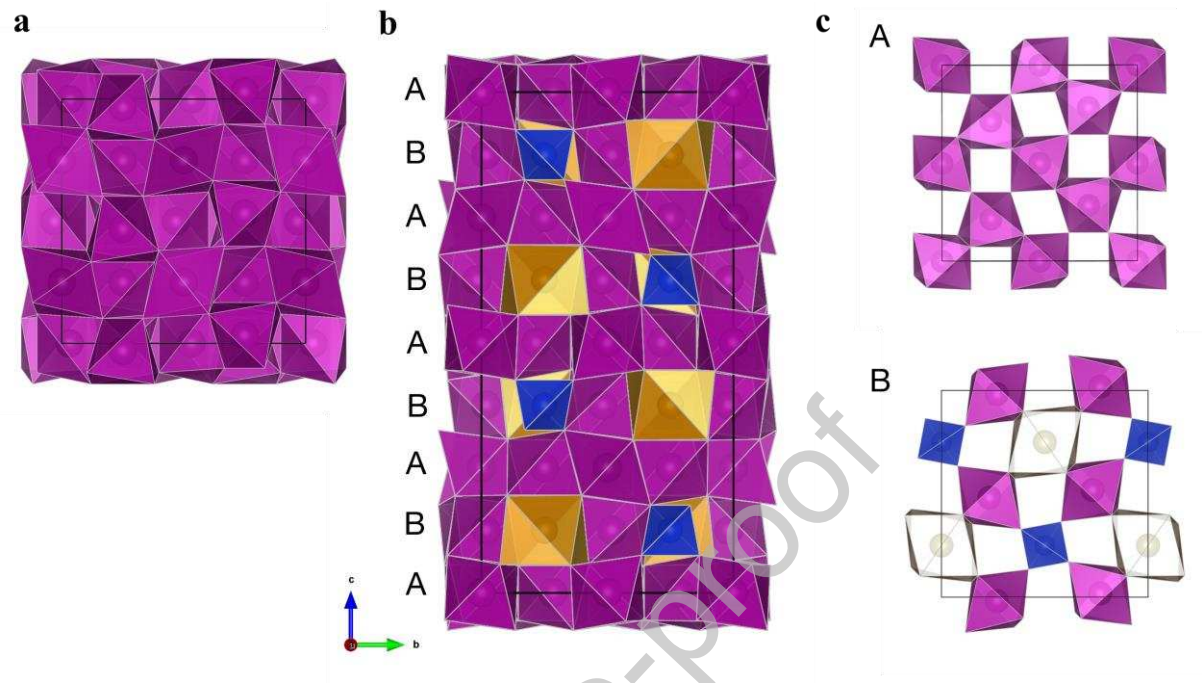


**Figure 1.** Crystal structures of (a) α-$Mn_2O_3$ (bixbyite) and of (b) $Mn_7SiO_{12}$ (braunite) viewed along a-axis (b) and the structure of its A and B slabs (c). Mn(III) cations are located in violet distorted octahedra, Mn(II) – in yellow distorted cubes and Si(IV) – in blue tetrahedra.

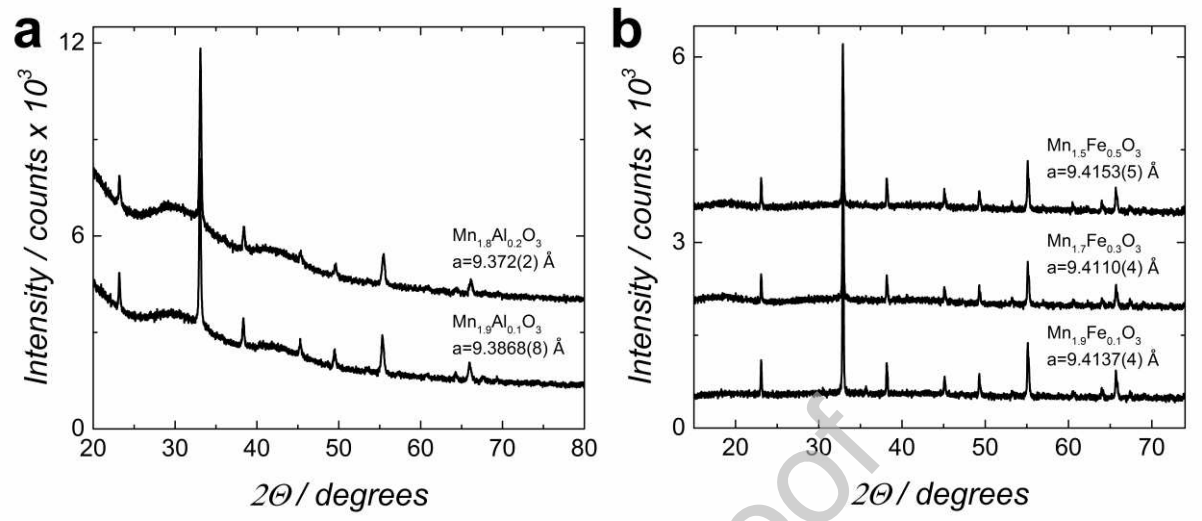


**Figure 2.** XRD patterns of $Mn_{2-x}Al_xO_3$**,** x= 0.1 and 0.2 (a) and $Mn_{2-x}Fe_xO_3$**,** x= 0.1, 0.3 and 0.5 (b) samples. Unit cell parameters are also shown.

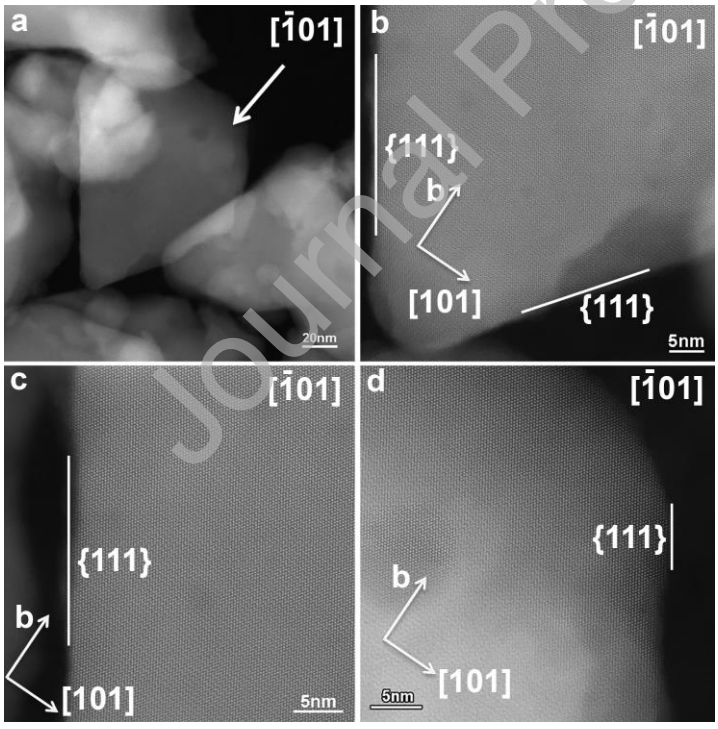


A

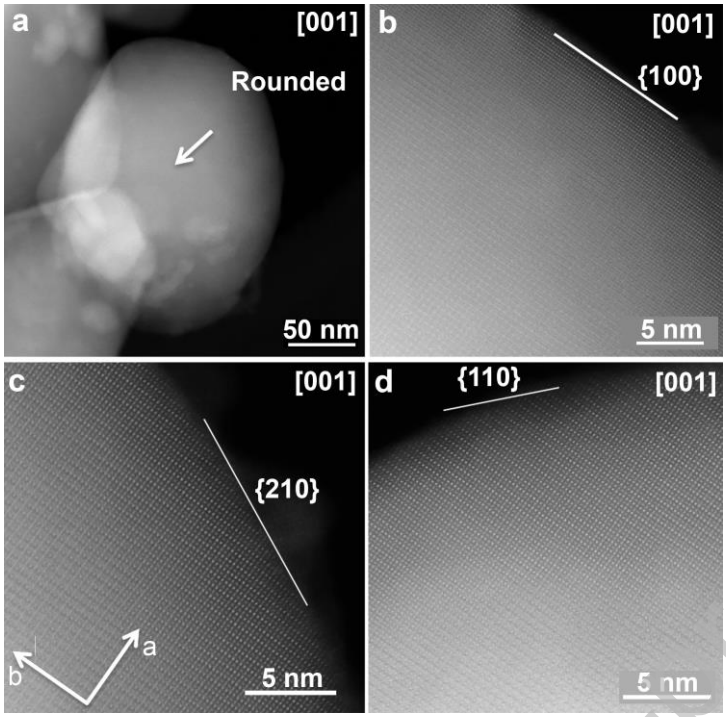


B

**Figure 3**. (**A**) HAADF-STEM image of a representative nanoparticle in the $Mn_2O_3$ (2) sample (a) and high resolution HAADF-STEM [-101] images from the different sides of this particle showing dominant {111} crystal planes at the surface (b, c and d). (**B**) HAADF-STEM image of a representative $Mn_{1.9}Fe_{0.1}O_3$ nanoparticle (a) showing the rounded shape (b, c and d). High resolution HAADF-STEM [001] images from different sides of this particle showing different crystal planes at the surface.

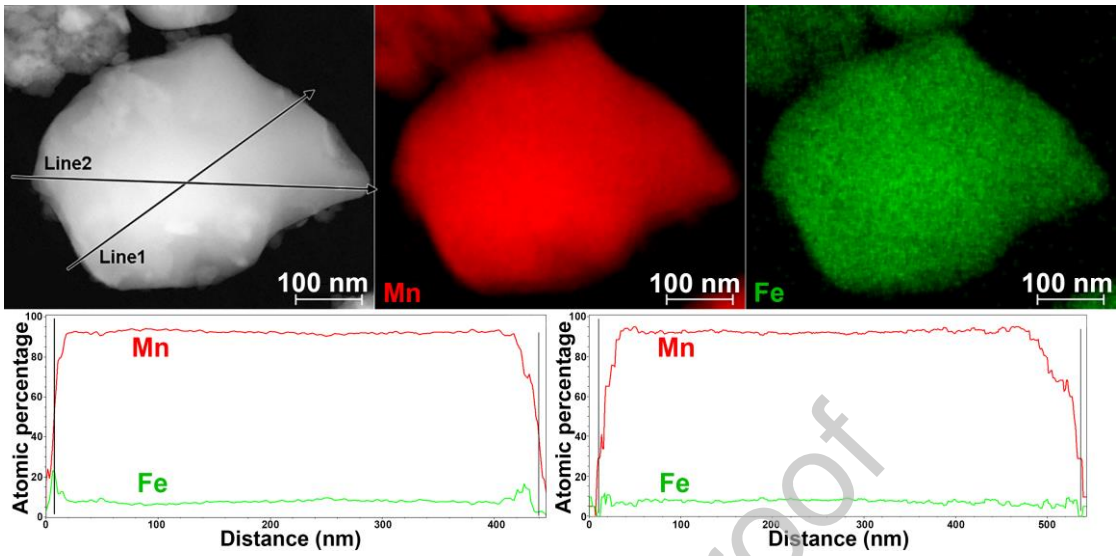


**Figure 4.** HAADF-STEM image and corresponding EDX maps and line profiles of a representative $Mn_{1.9}Fe_{0.1}O_3$ nanoparticle. The vertical black lines on the curves mark the borders of the particle as estimated from the HAADF-STEM image. The atomic percentage includes a contribution from the carbon support, which is not separately shown on the curve.

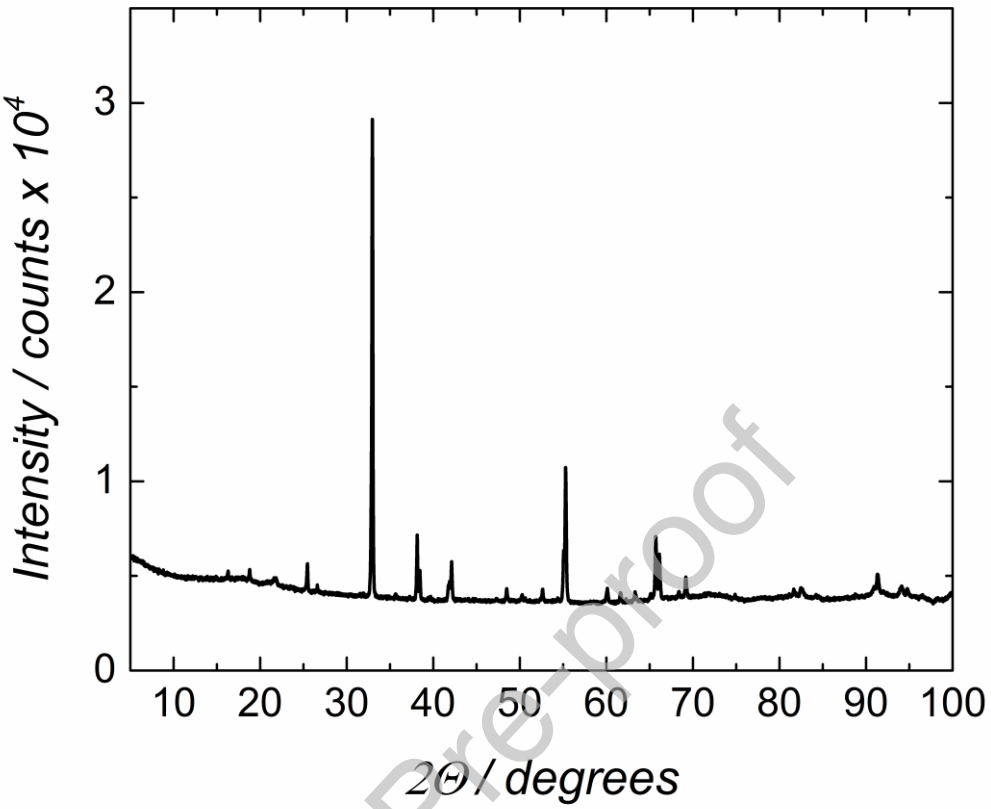


**Figure 5**. XRD pattern of $Mn_7SiO_{12}$ sample prepared by hydrolysis of $Mn(CH_3COO)_2$ and TEOS mixture with final annealing in air at 900 ℃ for 5h. Reflection positions for $Mn_7SiO_{12}$ from ICDD PDF #41-1367 are marked.

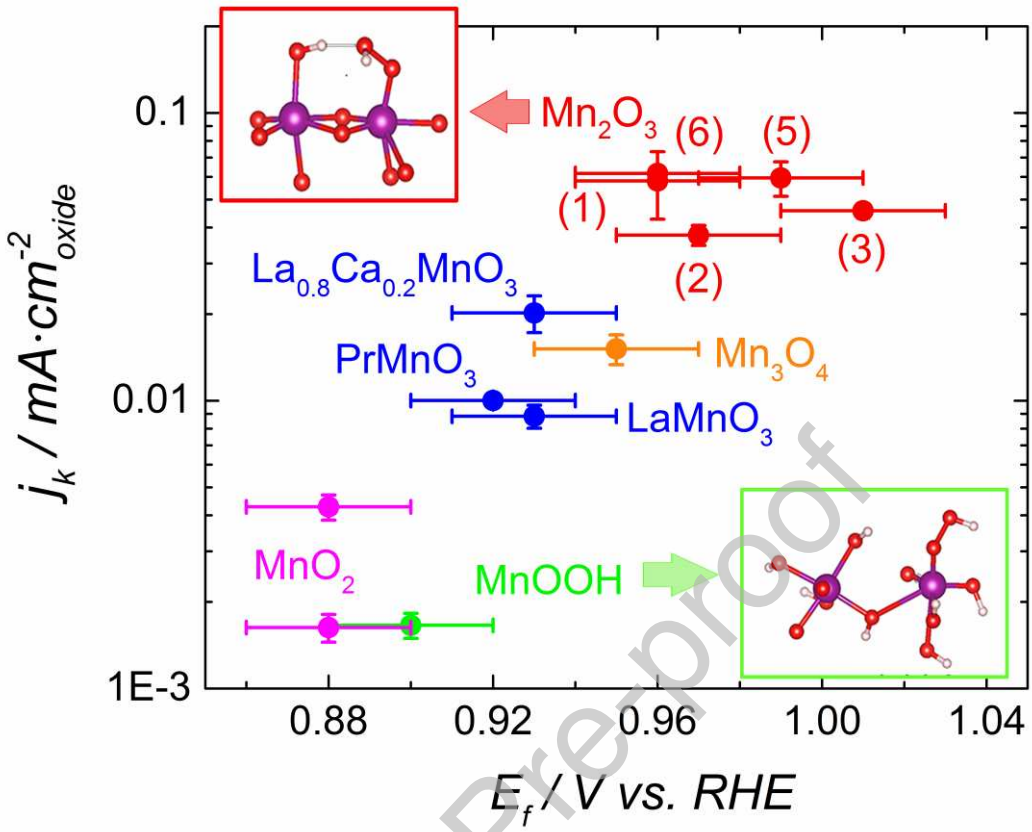


**Figure 6.** The kinetic ORR current at 0.9 V vs. RHE normalized to the BET area of oxide materials versus their corresponding formal potential of the Mn(IV)/Mn(III) surface red-ox transition. Color codes: red - $Mn_2O_3$ (numbers in brackets indicate the sample number), blue – Mn perovskites, orange - $Mn_3O_4$, magenta - β-$MnO_2$ (two data points refer to measurements with different cathodic limits, the lower value corresponding a lower cathodic limit), green - α-MnOOH. Adapted from Ref. 24. Inserts show $HO_2^-$ adsorbed on a α-$Mn_2O_3$ (red frame) and α-MnOOH (green frame) cluster. Adapted from Ref. 26.

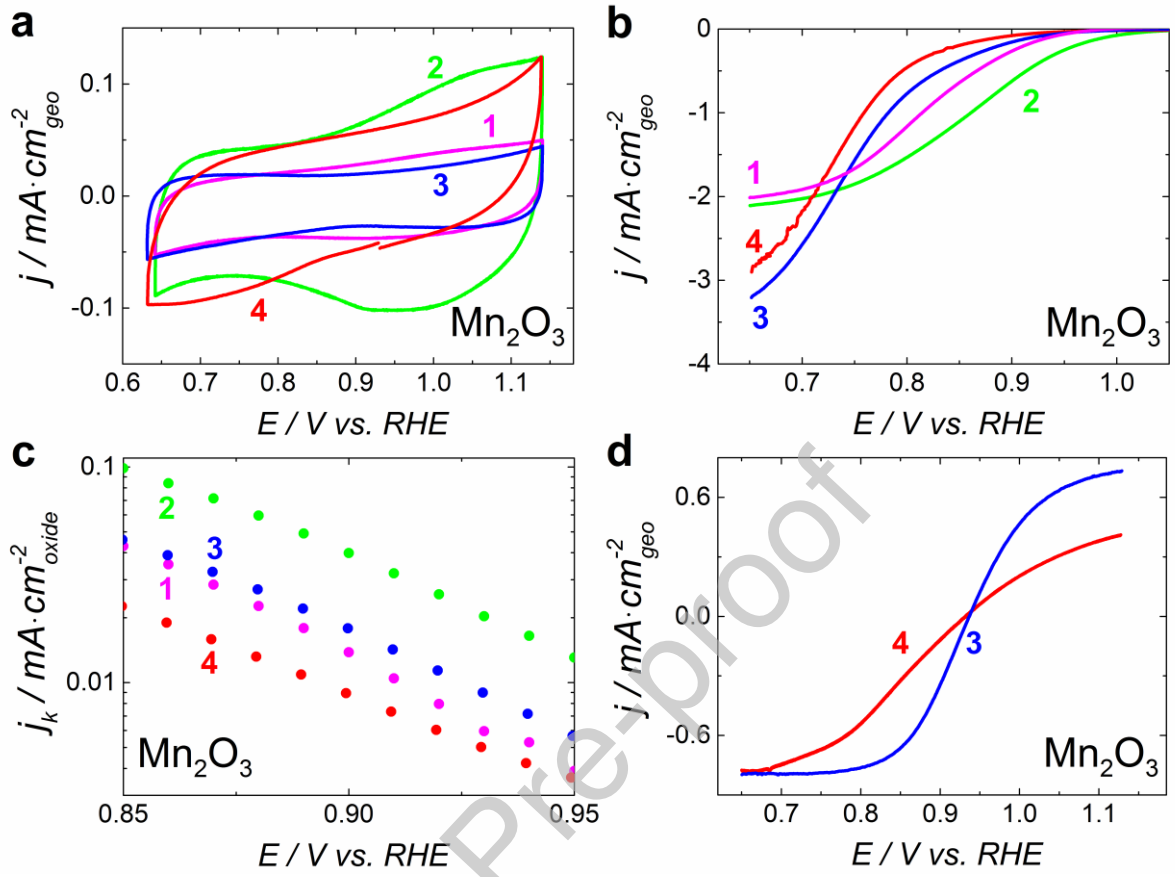


**Figure 7.** The CVs (a) and the positive scans of the RDE voltammograms (b, d) for GC-supported thin films of $Mn_2O_3$/C composites in $N_2$-purged (a), $O_2$-saturated (b) and $N_2$ -purged electrolyte containing 0.84 mM $H_2O_2$. Tafel plots constructed from RDE voltammograms presented in panel (b) are shown in panel (c). Curves '1' and '2' in panels (a, c) correspond to $Mn_2O_3$(3)/C ($S_{BET}$= 65 $m^2 \cdot g^{-1}$) in 1 M NaOH, curves '3' and '4' in panels (a, c) refer to $Mn_2O_3$(4)/C ($S_{BET}$= 6 $m^2 \cdot g^{-1}$) composites in 0.1 M KOH before ('3') and after ('4') potential hold at 0.3 V vs. RHE. Curves '3' and '4' in panel (d) refer to $Mn_2O_3$(3)/C ($S_{BET}$= 82 $m^2 \cdot g^{-1}$) composites in 1 M NaOH + 0.84mM $H_2O_2$ before (3) and after (4) potential hold at 0.3 V vs. RHE. Loading: 91 $\mu g \cdot cm^{-2}_{geo}$ for both $Mn_2O_3$ and carbon (1:1 ratio). Currents are normalized to the geometric area of the electrode (a, b, d) and corrected to the background currents measured in $N_2$ atmosphere (b, d). The kinetic ORR current are normalized to the BET surface area of $Mn_2O_3$ without subtraction of contribution of carbon (c).

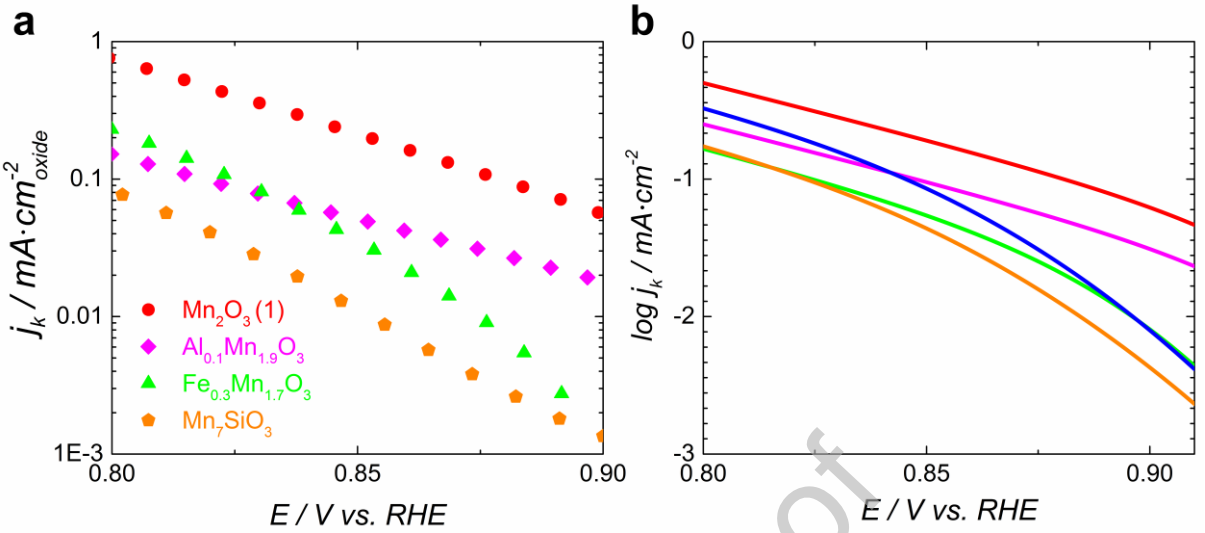


**Figure 8.** (a) The Tafel plots for GC-supported thin films of oxide/carbon composites recalculated from RDE voltammograms measured in $O_2$-saturated 1 M NaOH at 10 mV·s$^{-1}$ and 900 rpm. Loading: oxide is 91 µg·cm$^{-2}_{geo}$, carbon is 91 µg·cm$^{-2}_{geo}$. The kinetic ORR currents (a) are normalized to the BET surface area of oxides without subtracting contribution of carbon. (b) Simulated Tafel plots (b): red curve: $Q$= 0.1 mC cm$^{-2}$: $E_f$= 0.98 V, $k_5$= 50 s$^{-1}$, $k_2$= 1.5 10$^{13}$ mol$^{-1}$·cm$^3$ s$^{-1}$, $k_{-2}$= 1.7 10$^{-6}$ s$^{-1}$, $k_3$= 5.1 10$^{10}$ s$^{-1}$, $k_{-3}$= 4.9 10$^{-6}$ s$^{-1}$; magenta curve: $Q$= 0.05 mC·cm$^{-2}$, $E_f$= 0.98 V, $k_5$= 50 s$^{-1}$, $k_2$= 1.5 10$^{13}$ mol$^{-1}$·cm$^3$ s$^{-1}$, $k_{-2}$= 1.7 10$^{-6}$ s$^{-1}$, $k_3$= 5.1 10$^{10}$ s$^{-1}$, $k_{-3}$= 4.9 10$^{-6}$ s$^{-1}$; orange curve: $Q$= 0.085 mC cm$^{-2}$, $E_f$= 0.86 V, $k_5$= 0.5 s$^{-1}$, $k_2$= 0.75 10$^{13}$ mol$^{-1}$·cm$^3$ s$^{-1}$, $k_{-2}$= 0.65 10$^{-6}$ s$^{-1}$, $k_3$= 2.55 10$^{10}$ s$^{-1}$, $k_{-3}$= 2.45 10$^{-6}$ s$^{-1}$; green curve: $Q$= 0.085 mC·cm$^{-2}$, $E_f$= 0.86 V, $k_5$= 0.5 s$^{-1}$, $k_2$= 1.5 10$^{13}$ mol$^{-1}$·cm$^3$ s$^{-1}$, $k_{-2}$= 1.7 10$^{-6}$ s$^{-1}$, $k_3$= 5.1 10$^{10}$ s$^{-1}$, $k_{-3}$= 4.9 10$^{-6}$ s$^{-1}$; blue curve: $Q$= 0.085 mC·cm$^{-2}$, $E_f$= 0.86 V, $k_5$= 50 s$^{-1}$, $k_2$= 1.5 10$^{13}$ mol$^{-1}$·cm$^3$ s$^{-1}$, $k_{-2}$= 1.7 10$^{-6}$ s$^{-1}$, $k_3$= 5.1 10$^{10}$ s$^{-1}$, $k_{-3}$= 4.9 10$^{-6}$ s$^{-1}$. For other parameters see Table 1.

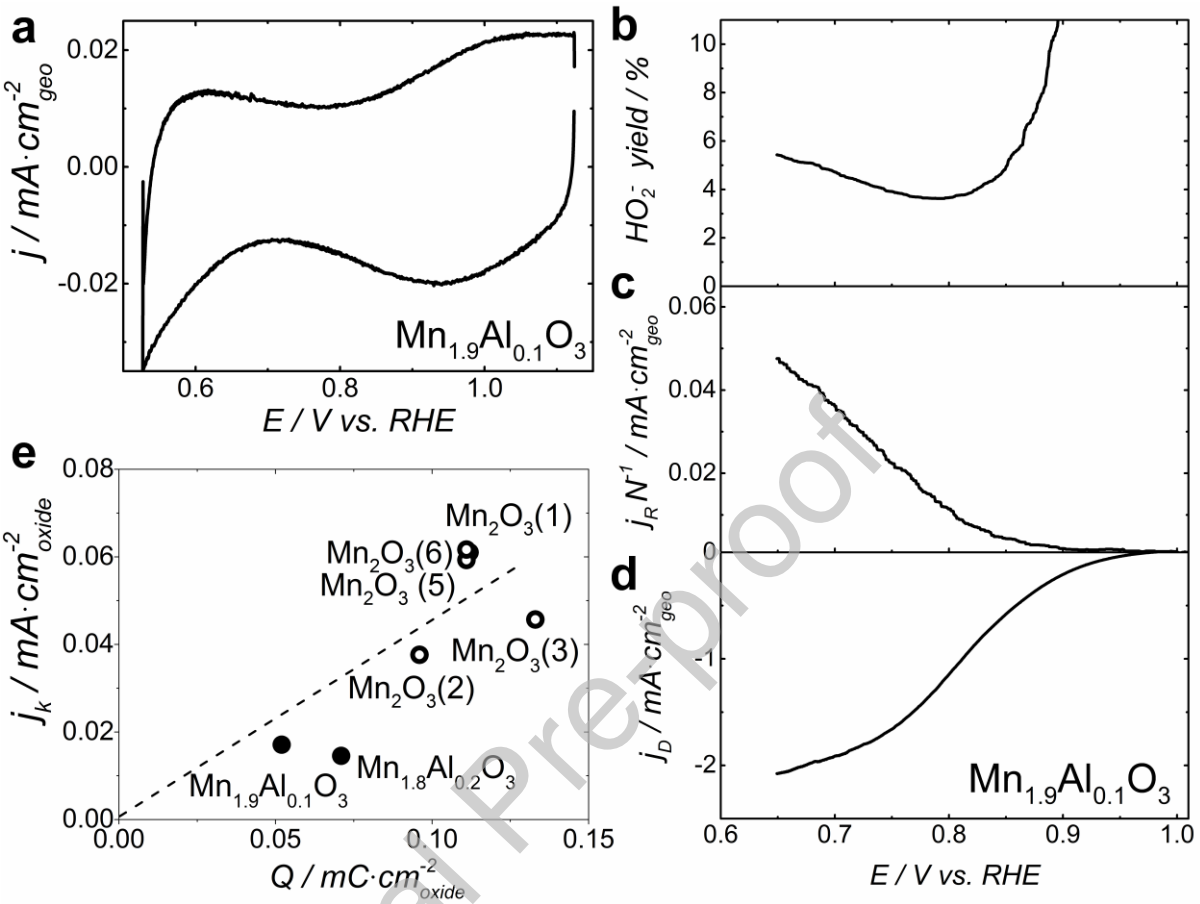


**Figure 9.** The CV in $N_2$-saturated (a) and RRDE data in $O_2$-saturated 1 M NaOH (b, c, d) for a GC-supported thin film of a $Mn_{1.9}Al_{0.1}O_3$/carbon composite with (b) percentage of $HO_2^-$ formed, (c) ring and (d) disk currents versus disk potential extracted from the positive scans of the RRDE voltammograms. Sweep rate 10 mV·s$^{-1}$. Rotation rate 0 (a) and 900 (b, c, d) rpm. Loading: oxide is 91 µg·cm$^{-2}_{geo}$, carbon ($S_{BET}$= 65 m$^2$·g$^{-1}$) is 91 µg·cm$^{-2}_{geo}$. Currents are normalized to the geometric area of the electrode (a, d) after subtraction of the carbon contribution (a) and correction to the background currents measured in the $N_2$ atmosphere (d). Ring currents in (c) are normalized to the geometric area of the disk electrode and to the collection factor. (e) Kinetic ORR currents for undoped and Al-doped $Mn_2O_3$ at 0.85 V vs. RHE plotted vs. their corresponding total change measured as explained in the experimental section.

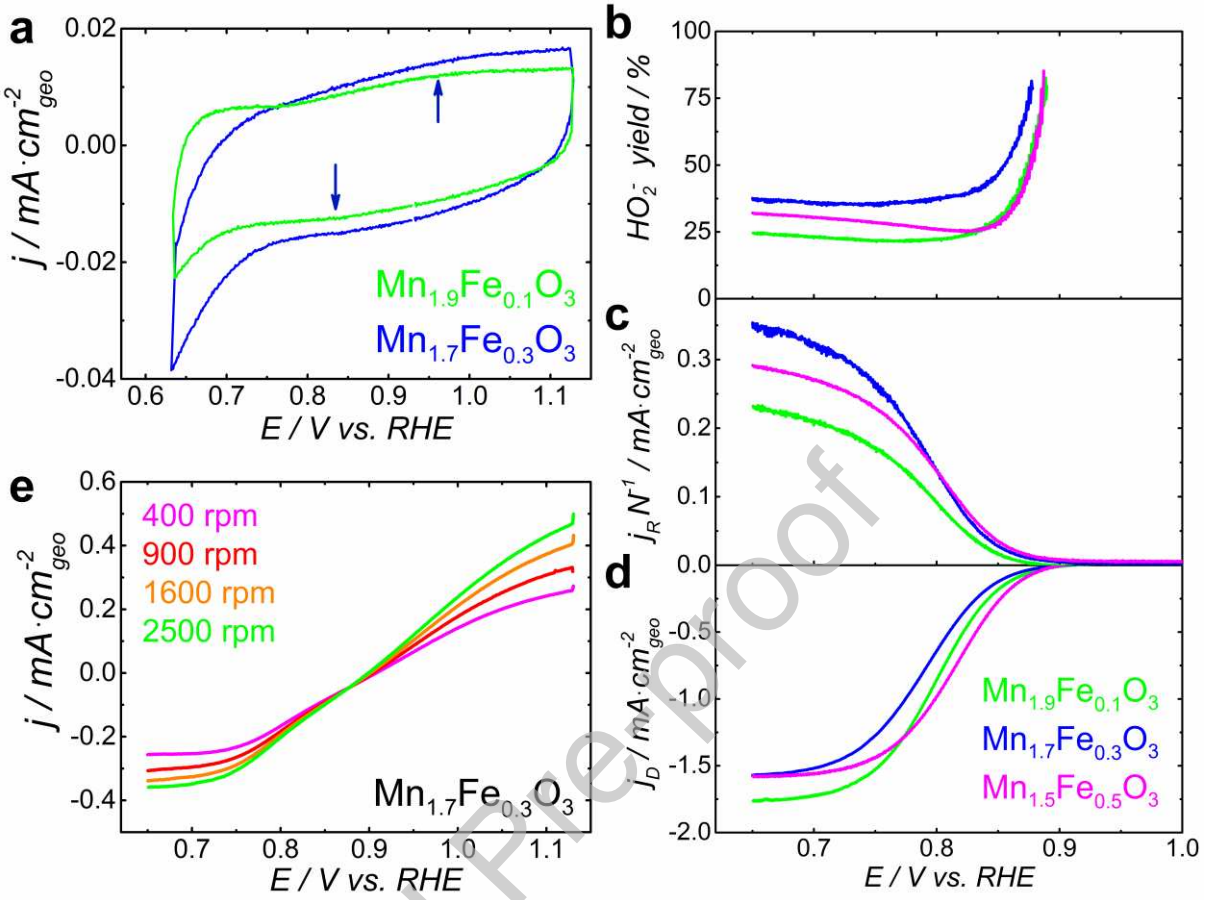


**Figure 10.** (a) The CV in $N_2$-saturated (a) and RRDE data in $O_2$-saturated 1 M NaOH (b, c, d) for GC-supported thin films of $Mn_{2-x}Fe_xO_3$/carbon composites (b) Percentage of $HO_2^-$ formed, (c) ring and (d) disk currents versus disk potential extracted from the positive scans of the RRDE voltammograms. Sweep rate 10 mV·s$^{-1}$. Rotation rate 0 (a) and 900 (b, c, d) rpm. Arrows in (a) indicate positions of the anodic and cathodic peaks. (e) RDE voltammograms for GC-supported thin films of $Mn_{1.7}Fe_{0.3}O_3$/carbon composites in 1 M NaOH + 0.84 mM $H_2O_2$ at 10 mV·s$^{-1}$. Loading: oxide is 91 µg·cm$^{-2}_{geo}$, carbon ($S_{BET}$= 65 m$^2$·g$^{-1}$) is 91 µg·cm$^{-2}_{geo}$. Currents are normalized to the geometric area of the electrode (a, d) after subtraction of the carbon contribution (a) and correction to the background currents measured in the $N_2$ atmosphere (d). Ring currents in (c) are normalized to the geometric area of the disk electrode and to the collection factor.

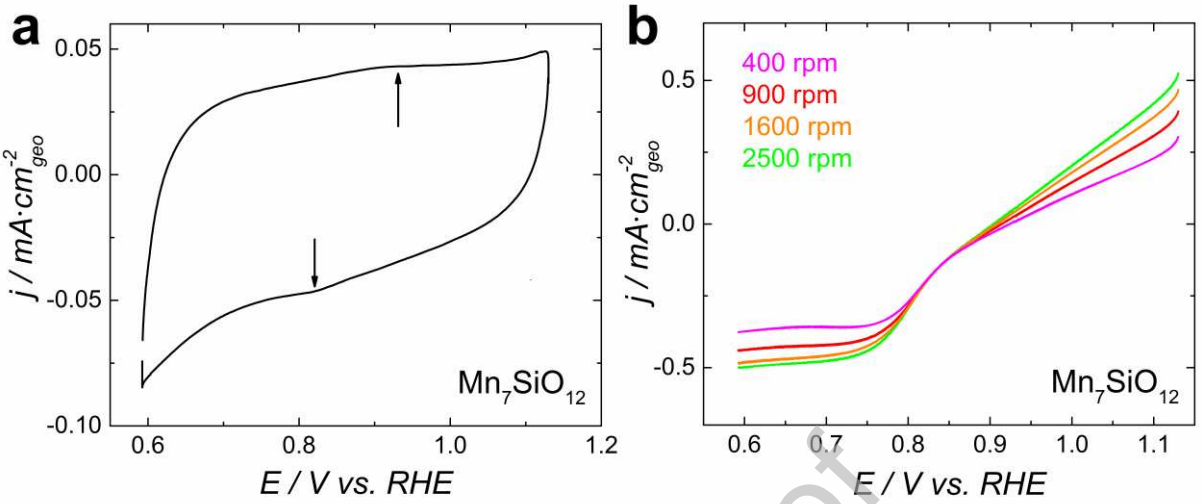


**Figure 11.** The CVs (a) and the positive scans of the RDE voltammograms (b) for GC-supported thin films of $Mn_7SiO_{12}$/carbon composites in $N_2$-purged 1 M NaOH (a) and 1 M NaOH +0.84 mM $H_2O_2$ (b) at 10 mV·s$^{-1}$. Loading: oxide is 91 µg·cm$^{-2}_{geo}$, carbon is 91 µg·cm$^{-2}_{geo}$. Currents are normalized to the geometric area of the electrode and corrected to the background currents measured on carbon under the same conditions (a) or to the background currents measured in $N_2$ atmosphere (b).

**Table 1.** Parameters used for the simulations of the current-potential curves.

| Parameter | Meaning | Units | Value |
|---|---|---|---|
| $E_f$ | Mn(IV/III) redox potential | V | *cf.* Figure caption |
| $k_1$ | Rate constant of step (1) | $s^{-1}$ | 0.2 |
| $k_2$ | $O_2$ adsorption rate constant | $cm^3 \cdot mol^{-1} \cdot s^{-1}$ | *cf.* Figure caption |
| $k_{-2}$ | $O_{2,ad}$ desorption rate constant | $s^{-1}$ | *cf.* Figure caption |
| $k_3$ | $O_{2,ad}$ reduction rate constant | $s^{-1}$ | *cf.* Figure caption |
| $k_{-3}$ | $HO_{2,ad}$ oxidation rate constant | $s^{-1}$ | *cf.* Figure caption |
| $k_4$ | $HO_2^-$ adsorption rate constant | $cm^3 \cdot mol^{-1} \cdot s^{-1}$ | $5 \cdot 10^7$ |
| $k_{-4}$ | $HO_{2,ad}$ desorption rate constant | $s^{-1}$ | 50 |
| $k_5$ | $HO_{2,ad}$ dissociation rate constant | $s^{-1}$ | *cf.* Figure caption |
| $F$ | Faraday constant | $C \cdot mol^{-1}$ | 96485 |
| $R$ | Gas constant | $J \cdot K^{-1} \cdot mol^{-1}$ | 8.314 |
| $T$ | Temperature | K | 300 |
| $C_{O_2}^b$ | $O_2$ bulk concentration | $mol \cdot cm^{-3}$ | $0.84 \cdot 10^{-6}$ |
| $\alpha$ | Charge transfer coefficient | | 0.5 |

**Table 2.** The ratio Mn:A in $Mn_{2-x}A_xO_3$, A=Fe, Al calculated from XPS data[(i)].

| **Mn:A ratio** | **$Mn_{1.9}Al_{0.1}O_3$** | **$Mn_{1.8}Al_{0.2}O_3$** | **$Mn_{1.9}Fe_{0.1}O_3$** | **$Mn_{1.7}Fe_{0.3}O_3$** | **$Mn_{1.5}Fe_{0.5}O_3$** |
|---|---|---|---|---|---|
| Stoichiometric | 19 | 9 | 19 | 5.67 | 3 |
| Calculated from XPS | 4.5±0.9 | 1.8±0.4 | 20±8[(ii)] | 7.9±1.6 | 4.8±1 |

[(i)]XPS spectra can be found in the Supplementary Information.
[(ii)]High error due to the low intensity of the Fe2p signal.

**Table 3.** Characterization data for the samples under study. $E_f$ is the formal potential of Mn(IV/III) interfacial redox transition. $Q$ is the total charge with cathodic limit 0.65 V vs. RHE (measured at 10 $mV \cdot s^{-1}$, averaged for anodic and cathodic branches after subtraction of the charge originating from carbon, and normalized to the oxide BET surface area). $Q_{calc}$ is the specific charge expected for recharging of all surface Mn cations (see Section 2.3 for detail). $j_k$ is kinetic ORR current density at 0.85 V vs. RHE normalized to the oxide BET surface area without subtraction of carbon contribution.

| **Sample** | **BET, $m^2 \cdot g^{-1}$** | **$E_f$, V vs. RHE** | **$Q$, $mC \cdot cm^{-2}_{oxide}$** | **$Q_{calc}$,[(i)] $mC \cdot cm^{-2}_{oxide}$** | **$j_k$, $\mu A \cdot cm^{-2}_{oxide}$ at 0.85 V** |
|---|---|---|---|---|---|
| $Mn_2O_3$ (1) | 3 | 0.96 ± 0.02 | 0.111 ± 0.009 | 0.182 | 212 ± 5 |
| $Mn_2O_3$ (2) | 10 | 0.97 ± 0.02 | 0.096 ± 0.003 | 0.182 | 112±8 |
| $Mn_2O_3$(3) | 24 | 1.01 ± 0.02 | 0.133 ± 0.001 | 0.182 | 116 ± 8 |
| $Mn_2O_3$(4)[(ii)] | 10 | - | - | 0.182 | 19±2 |
| $Mn_2O_3$(5) | 8 | 0.99 ± 0.02 | 0.112 ± 0.006 | 0.182 | 190±13 |
| $Mn_2O_3$(6) | 27 | 0.96 ± 0.02 | 0.111 ± 0.001 | 0.182 | 165±3 |
| $Mn_{1.9}Fe_{0.1}O_3$ | 3 | 0.89± 0.05 | 0.180 ± 0.010 | 0.176 | 63± 4 |
| $Mn_{1.7}Fe_{0.3}O_3$ | 3 | 0.91± 0.05 | 0.160 ± 0.010 | 0.163 | 42± 7 |
| $Mn_{1.5}Fe_{0.5}O_3$ | 4 | - | 0.460 ± 0.020 | 0.150 | 67± 8 |
| $Mn_{1.9}Al_{0.1}O_3$ | 15 | 0.98 ± 0.02 | 0.052 ± 0.003 | 0.177 [0.149] | 50± 3 |
| $Mn_{1.8}Al_{0.2}O_3$ | 15 | 0.97 ± 0.02 | 0.071 ± 0.002 | 0.171 [0.117] | 49± 4 |
| $Mn_7SiO_{12}$ | 23 | 0.86 ± 0.03 | 0.095 ±0.005 | 0.150 [0.116][(iii)] | 11±1 |

[(i)]For Fe (Al) doped oxides the charge is calculated assuming red-ox inactivity of the doping element in the studied potential interval and considering bulk fraction of the doping element. The charge value in the brackets is calculated considering surface fraction of Mn determined from XPS (Table 2).

[(ii)]The data were obtained in 0.1 M KOH using Sibunit carbon with low surface area (BET 6 $m^2 \cdot g^{-1}$), which does not allow maximizing the accessibility of the oxide surface and thus results in a lower ORR activity of $Mn_2O_3$/C composite (for more information see [53]).

[(iii)]The first value corresponds to the charge of all surface Mn(III) cations, while the value in the brackets only considers the charge associated with recharging of Mn(III) from the A-slab of the braunite structure.